Nanoscale

REVIEW

View Article Online
View Journal | View Issue

Cite this: *Nanoscale*, 2021, **13**, 19712

Two-dimensional materials for electrochemical CO_2 reduction: materials, *in situ*/*operando* characterizations, and perspective

Zuolong Chen,† Xiyang Wang, † Joel P. Mills, Cheng Du, Jintae Kim, John Wen and Yimin A. Wu *

Electrochemical CO_2 reduction (CO_2 ECR) is an efficient approach to achieving eco-friendly energy generation and environmental sustainability. This approach is capable of lowering the CO_2 greenhouse gas concentration in the atmosphere while producing various valuable fuels and products. For catalytic CO_2 ECR, two-dimensional (2D) materials stand as promising catalyst candidates due to their superior electrical conductivity, abundant dangling bonds, and tremendous amounts of surface active sites. On the other hand, the investigations on fundamental reaction mechanisms in CO_2 ECR are highly demanded but usually require advanced *in situ* and *operando* multimodal characterizations. This review summarizes recent advances in the development, engineering, and structure–activity relationships of 2D materials for CO_2 ECR. Furthermore, we overview state-of-the-art *in situ* and *operando* characterization techniques, which are used to investigate the catalytic reaction mechanisms with the spatial resolution from the micron-scale to the atomic scale, and with the temporal resolution from femtoseconds to seconds. Finally, we conclude this review by outlining challenges and opportunities for future development in this field.

Received 20th September 2021,
Accepted 10th November 2021

DOI: 10.1039/d1nr06196h

rsc.li/nanoscale

1 Introduction

The historically unprecedented atmospheric CO_2 levels of current times have resulted in global warming and extinction risks to many animal and plant species.[1,2] Therefore, the fixation and conversion of CO_2 is critical in realizing energy and

Department of Mechanical and Mechatronics Engineering, Waterloo Institute for Nanotechnology, Materials Interface Foundry, University of Waterloo, Waterloo, Ontario N2L 3G1, Canada. E-mail: yimin.wu@uwaterloo.ca
†These authors contributed equally to this work.

Zuolong Chen

Zuolong Chen graduated from the University of Toronto in 2020 with a MASc degree and joined Prof. Yimin Wu's group at the University of Waterloo to pursue his doctoral studies in 2021. His research focuses on the syntheses and applications of nanomaterials and thin films for the electrocatalytic and photocatalytic conversions of CO_2 to valuable fuels.

Xiyang Wang

Xiyang Wang received his BS degree (2014) and Ph.D. degree (2019) in the Department of Chemistry at Jilin University. After that, he worked as a postdoctoral fellow at Jilin University in 2019. Currently, he is working as a postdoctoral fellow under the supervision of Professor Yimin Wu in the Department of Mechanical and Mechatronics Engineering at the University of Waterloo. His research interests focus on the structural design and structure–activity relationships in transition metal oxides (powders and thin films) applied in CO_2 reduction and automotive exhaust purification.

environmental sustainability. Over the past decades, many CO_2 reduction reaction (CO_2RR) strategies have been developed to produce high-value fuels or commodity chemicals to address this problem. Among these approaches, the electrochemical CO_2 reduction (CO_2 ECR) is a well-studied strategy that employs electrochemical electrolyzers to convert CO_2 to value-added fuels using renewable energy and electrochemical catalysts. Compared to other CO_2 conversion approaches, CO_2 ECR has attracted great attention due to many of its advantages: (1) mild work environment at room temperature and atmospheric pressure, (2) the ability to yield various high-value-added chemicals, especially HCOOH, CO, CH_4, CH_3OH, CH_3CH_3OH, C_2H_4, *etc.* (3) tunable chemical reactions – parameters such as electrolytes, operating voltage, and reactants can be easily adjusted based on the desired reactions, (4) the potential to utilize renewable energy as the energy source and industrial waste as the reactants, and (5) variety of available options for reactor designs.[3–5] However, in CO_2RR, molecule CO_2 is chemically inert that the activation of the C═O bond in CO_2 requires high overpotentials and high energy at 750 kJ mol^{-1}.[6] Further complicating the reaction, the highly intricate electrochemical CO_2 reduction processes occur in an aqueous environment and involve multiple electrons and protons transfer in various reaction paths, producing a wide variety of chemical products.[6,7] To this day, the mass production of multicarbon CO_2RR products, such as ethanol and ethylene, is still challenging and far from real-life applications, as only the catalysts with superior morphological and electronic structure are capable of achieving such highly demanded reactions.[6,8,9] The adsorption, interaction, and desorption of CO_2 and multiple reaction intermediates on catalyst surfaces are the key steps in CO_2 ECR processes and are determined by such catalyst properties.[10] Therefore, engineering low-cost, green electrocatalysts with excellent durability, high activity, and desired selectivity is crucial in developing the next-generation CO_2 reduction reaction (CO_2RR) applications.

The demand for high-efficiency catalysts for electrochemical CO_2RR has stimulated tremendous research efforts in the field.[9] Over the past decades, the research focus shifted from bulk materials to nanomaterials and then from nanomaterials to advanced two-dimensional materials. Early works on the subject focused on metal bulk materials such as Cu, Au, Pd, and Ag, which all demonstrated the catalytic activities of such catalysts to convert CO_2 into hydrocarbons, CO, methanol, *etc.* However, the activity, durability, and selectivity of these catalysts are low for CO_2 reduction to meet practical demand.[11–15] To address these shortcomings, the rapid development of CO_2RR nanocatalysts has improved the performance of CO_2RR in the catalytic activity, selectivity, and stability due to a large amount of surface active sites of nanocatalysts.[16–20] However, the current state-of-the-art systems are still far from practical applications.

Ultra-thin two-dimensional (2D) catalysts with atomic-scale thicknesses have demonstrated outstanding capabilities and performance as CO_2 ECR catalysts. Compared with nanoparticles and their bulk materials, 2D materials are excellent catalyst candidates, owing to their intrinsic advantages such as ultrahigh specific surface area, abundant exposed surface atoms, atomically flat facet, and high electrical conductivity.[3,21,22] Many structural, chemical, and electronic properties can be fine-tuned based on the desired reaction paths and products *via* various strategies, including defect engineering, doping, surface structural modification, and surface functionalization.[23–27] On the other hand, the study of 2D catalysts for CO_2RR can also help us understand the relationships between active sites and the catalysis mechanism and performance at the atomic scale.[3] Hence 2D solids are usually considered as an ideal model catalyst to study CO_2RR mechanisms. The emergence of 2D materials offers a promising opportunity for the further development and applications of electrochemical CO_2 reduction.

Meanwhile, *in situ* and *operando* characterizations have become the essential tools to understand CO_2 RR mechanisms and evaluate catalyst performance. The electrocatalytic reductions of CO_2 are extremely complicated: multiple reaction pathways can lead to the generations of various reaction intermediates and products, requiring the transfer of multiple protons and electrons. During CO_2 reduction reactions,

Joel P. Mills

Joel P. Mills graduated from the University of Waterloo with a Bachelor's degree in Mechanical Engineering in 2020 and currently is a Master student working in catalyst and cell design for CO_2 conversion under the supervision of Professor Yimin Wu at the University of Waterloo.

Cheng Du

Cheng Du received his Ph.D. in analytical chemistry from Changchun Institute of Applied Chemistry, Chinese Academy of Sciences (2019). He has been a postdoc in Prof. Yimin Wu's group at the University of Waterloo since 2020. He was also co-supervised by Professor John Wen. His research interests include the controllable synthesis of nanomaterials and their application in electrocatalysis and photocatalysis.

advanced *in situ* and *operando* characterizations can monitor the generations of both reaction intermediates and products, identify catalytic active sites under the real time, probe the state and properties of catalysts, and reveal the reaction pathways in dynamic reaction environment.[28,29] While many such advanced techniques have been developed and widely utilized for CO_2 ECR studies, new concepts and techniques have attracted much attention for the discoveries of novel catalysts and studies of fundamental reaction mechanisms.

In this review, we summarize the research progress on four types of representative 2D materials employed in electrochemical CO_2RRs: (1) transition metals (TMs), (2) transition metal oxides (TMOs), (3) transition metal dichalcogenides (TMDs), and (4) other types of 2D materials (MXenes, metal organic framework, covalent organic frameworks). Then, we describe current regulating strategies and structure–activity correlations of 2D materials for electrocatalytic CO_2RR. In addition, several state-of-the-art *in situ* and *operando* characterization techniques are reviewed. Finally, this review will conclude with a perspective on upcoming challenges, opportunities, and trends of 2D materials of future 2D electrochemical CO_2 reduction catalysts research.

2 Nanostructured two-dimensional materials for CO_2 electroreduction

To date, numerous two-dimensional (2D) materials have been developed and utilized in CO_2 ECR applications, leading to many exciting and promising findings and material candidates. In general, there are five categories of 2D materials that have demonstrated promising CO_2 ECR performance: a. 2D transition metals, b. 2D transition metal oxides, c. 2D transition metal dichalcogenides (TMDs), d. 2D carbon-based materials, and e. metal–organic frameworks and covalent organic frameworks. Fig. 1 shows representative transmission electron microscopy (TEM) and atomic force microscopy (AFM) images of these five categories of 2D materials reviewed in this article.

2.1 Two-dimensional 2D transition metals (TMs)

Transition metals have been extensively studied for CO_2RR for decades.[35] Notably, transition metal nanosheets are highly effective electrocatalysts for CO_2 ECR due to their abundant active sites and high conductivity.[36] Such advantages can benefit CO_2 ECR *via* different mechanisms. By optimizing the electronic properties, Bi nanosheets have exhibited high selectivity towards formic acid in CO_2RR and a high faradaic efficiency of 92% in 0.5 M $KHCO_3$ solution at ~1.5 V (*versus* SCE). Such 2D nanosheets also generated lower onset potential and about five times higher current density compared to commercial Bi nanoparticles.[37] Density functional theory (DFT) calculations proved that 10 nm-thick Bi nanosheets have a higher density of states (DOS) at the Fermi level than bulk Bi, leading to improved CO_2RR performance with high selectivity and excellent stability for electrocatalysis CO_2 reduction.[38] The morphological advantages of 2D TMs have also enhanced CO_2 ECR performance. DFT calculations for Bi nanosheets synthesized *via* a molten-salt-assisted method suggested that the edge sites of Bi nanosheets demonstrate superior activity than terrace sites.[39] In terms of surface properties, Bi nanosheets obtained by liquid-phase exfoliate method exhibited greater hydrophilicity than Bi bulk materials, thus promoting the electron transfer between solid and liquid. These Bi nanosheets produced a high current density of 16.5 mA cm^{-2} at −1.1 V (*versus* RHE), a faradaic efficiency of 86.0% for formate production, and well-preserved catalytic activity after 10 h of testing.[36] In addition, advanced 2D structures have shown promising performance in CO_2 ECR. 2D mesoporous Bi nanosheets prepared *via* the cathodic conversion method

Jintae Kim

Jintae Kim is a mechanical engineering undergraduate at the University of Waterloo. To pursue his interest in materials engineering, he has joined Prof. Yimin Wu's group at the University of Waterloo as co-operative program student.

John Wen

Prof John Wen is a Professor in the Department of Mechanical & Mechatronics Engineering and cross-appointed in the Department of Chemical Engineering at the University of Waterloo. He is the director of the Waterloo Laboratory for Emerging Energy Research (LEER) and has already worked in a multidisciplinary field for developing novel energy technologies focusing on nanotechnology and renewables. Prior to Waterloo he was a postdoctoral fellow at the Massachusetts Institute of Technology where he worked with the Green group at Chemical Engineering for modeling combustion and reaction kinetics.

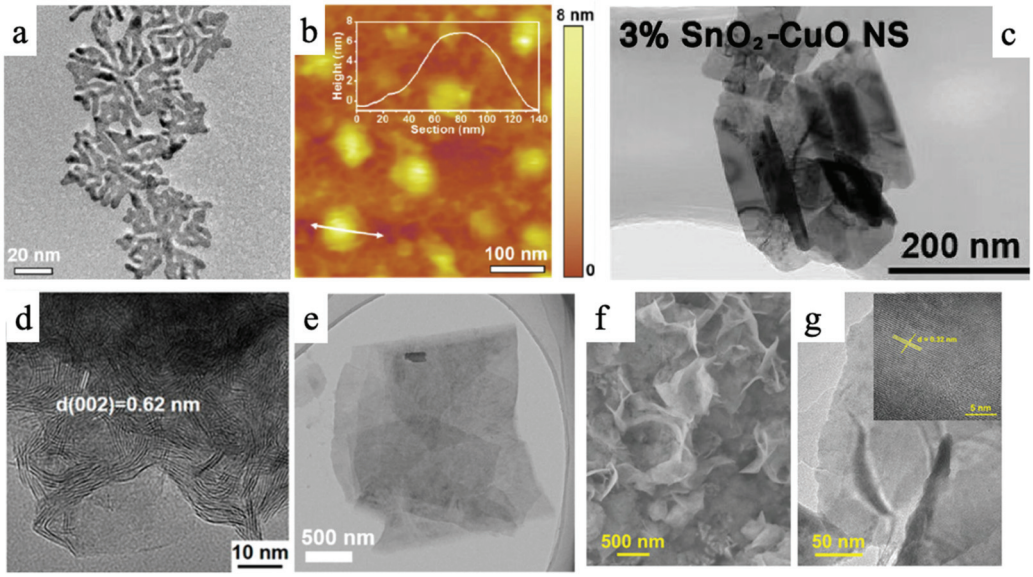

Fig. 1 An overview of different types of 2D materials. (a) and (b) TEM and AFM images of 2D palladium–copper alloy nanodendrites; (c) SnO_2 modified two-dimensional CuO nanosheet; (d) TEM image of MoS_2 nanosheet; (e) TEM image of Ultrathin 2D Mxene. (f) and (g) TEM images of Bi-MOF ultrathin nanosheet.[30–34]

demonstrated a large current density of ~18 mA cm^{-2} at −1.1 V, a high faradaic efficiency for formate conversion of almost 100%, and an excellent durability of 12 h.[40] A recent report of hydrangea-like superstructure consisting of ultrathin Bi nanosheets demonstrated a faradaic selectivity of over 95% with a wide potential window ranging from −0.78 V to −1.18 V and a high current density of over 300 mA cm^2.[41]

In a recent report, 50 nm-thick Ag nanosheets with hierarchical structures demonstrated a large surface area for catalytic reactions and gas transport/diffusion, resulting in a high faradaic efficiency of 95% for CO_2 conversion into CO and a current density that is 37 times higher than that of Ag nanoparticles at −0.6 V (*versus* RHE).[42] Multilayered Zn nanosheets also showed high faradaic efficiency of ~86% for CO product at 1.13 V (*versus* RHE) and good stability during a 7-hour test. The high density in edge sites in Zn nanosheets resulted in a density 9 times higher than that of bulk Zn foil.[43] Ultrathin copper nanosheets prepared by galvanic replacement method also exhibited high selectivity and activity for CO_2 reduction, where the optimized hierarchical Cu electrodes possessed a faradaic efficiency of 74.1% for CO product and a current density of 23.0 mA cm^{-2} at −1.0 V (*versus* RHE).[44] Abundant vacancy defects in ultrathin Cu nanosheets can improve the initial kinetics of CO formation and accelerate the mass and electrons transport in the CO_2 reduction process. Moreover, hybrid Cu/$Ni(OH)_2$ nanosheets, which consist of atomically thick Cu nanosheets loaded on $Ni(OH)_2$, also displayed excellent activity, selectivity, and durability (22 hours) in electrocatalytic CO_2 reduction.[45] The nanosheets provided a large current density of 4.3 mA cm^{-2} at −0.5 V (*versus* RHE) and a high faradaic efficiency of 92% for CO product.[45] Ultrathin 2D hierarchical Pd/SnO_2 nanosheets, namely Pd nanosheets partially capped by SnO_2 nanoparticles, displayed a maximum faradaic efficiency (FE) of ~54.8% at −0.24 V (*versus* RHE) and high stability for electroreduction of CO_2 into CH_3OH.[46] The enhanced performance of Pd/SnO_2 nanosheets could be attributed to the abundance of Pd–O–Sn interfaces. Notably, recent advances in 2D alloys have demonstrated enhanced CO_2 ECR performance than their single-component counterparts. A palladium–copper alloy nanodendrite system exhibited a high Formate selectivity of over 90% at a low cathodic over potential of −0.4 V_{RHE}.[30] Fig. 1a and b demonstrate the morphology of this nanodenrite system. DFT calculations revealed that Cu

Yimin A. Wu

Prof. Yimin A. Wu obtained his DPhil in Materials from the University of Oxford in 2013. From 2013–2014, he worked as a SinBeRise Postdoctoral Fellow at the University of California and Lawrence Berkeley National Laboratory. From 2014–2018, he worked at Argonne National Laboratory. In 2018, he joined the faculty of University of Illinois and held a joint appointment at Argonne National Laboratory. Since July 2019, he has been a professor at the University of Waterloo. Professor Wu's research focuses on the design of materials interfaces for energy and enivormental materials; novel electronic, photonic, responsive materials; and energy efficient neuromorphic computing.

atoms can weaken the *CO adsorption to avoid CO surface poisoning and promote the *OCHO adsorption on neighboring Pd atoms.[30] Such synergistic effects shall inspire more research endeavors in 2D alloy systems in the future.

Ultrathin metal nanosheets are prone to oxidation, which leads to a rapid decay in cyclability. However, many studies have also demonstrated through theory calculations and various characterizations that MO_x layer on the surface of transition metals plays a vital role in electrocatalytic CO_2.[47–49] Recently, Xie *et al.* successfully prepared 4-atoms-thick Co nanosheets (~0.84 nm) with different surface structures by a ligand-confined growth strategy.[50] Partially oxidized Co nanosheets showed an onset potential of −0.68 V for formate production in 0.1 M Na_2SO_4 solution, a high current density of 10.59 mA cm^{-2}, a faradaic efficiency of 90.1% towards formate, and durability of over 40 h.[50] Furthermore, catalytic activity for these 4-atom-thick Co nanosheets showed a 260-fold improvement compared to bulk metal Co, stemming from a large number of surface active sites in ultrathin 2D nanosheets and the existence of surface Co oxides. Partially oxidized Co nanosheets with a smaller Tafel slope of ~59 mV dec^{-1} show a fast pre-equilibrium for the formation of intermediate $CO_2^{\bullet-}$, suggesting that surface Co oxide in nanosheets can accelerated CO_2 activation and facilitate the rate-determining step for H^+ transfer in chemical reaction.[50]

2.2 Two-dimensional 2D transition metal oxides (TMOs)

Transition metal oxides have been extensively studied for usage in photoelectrochemical and electrochemical CO_2 reduction reactions because of their controlled structure, tunable energy band gap, and low cost. Their unfilled orbitals and active d electrons can energetically facilitate the bonding between metal atoms and CO_2 molecules.[51] However, traditional bulk transition metal oxides' low specific surface area and poor electrical conductivity are two key drawbacks that limit their activity and stability in CO_2 reduction.[52] Therefore, the emergence of two-dimensional (2D) transition metal oxides provides a promising opportunity to develop CO_2 reduction reaction. It has been reported that 3D hierarchical SnO_2 nanosheets, at a moderate overpotential of 0.88 V, demonstrated a high faradaic efficiency of 87% for the production of formate and a partial current density of 45 mA cm^{-2}.[53] This outstanding performance stemmed from the large surface area and fast electron transfer in 2D nanosheets. 1.72 nm-thick Co_3O_4 nanosheets prepared by solvothermal reaction also exhibited high activity for electrocatalytic CO_2 reduction that the current density reached 0.68 mA cm^{-2} at −0.88 V (*versus* SCE).[53] The formate faradaic efficiency was over 60% in 20 h.[52] Based on this, engineered Vo-rich single-unit-cell layer Co_3O_4 possessed higher current densities of 2.7 mA cm^{-2} and 85% selectivity for formate product at −0.87 V (*versus* SCE).[54] DFT calculations and experiments demonstrated that abundant oxygen vacancies could promote the adsorption of CO_2 on Co_3O_4 and the desorption of $HCOO^-$, while further lowering the rate-limiting activation energy, leading to improvement in activity and durability in the catalytic reaction. Some other researchers also found that ZnO nanosheets with rich oxygen vacancies display a high current density of −16.1 mA cm^{-2} at −1.1 V (*versus* RHE) and a high faradaic efficiency of 83% for CO production compared with ZnO nanosheets and ZnO nanosheets with poor oxygen vacancies.[55] DFT calculations and various characterizations clarified that large surface specific area and rich oxygen vacancies could increase surface active sites and facility the activation of CO_2 molecular.[55] Up to now, many other ultrathin transition metal oxide nanosheets made of TiO_2,[56] WO_3,[57] Bi_2WO_6,[58] $ZnGa_2O_4$,[59] $SnNb_2O_6$,[60] or $BiVO_4$[61] have been successfully prepared *via* a variety of methods and these 2D materials all also exhibited excellent performance for photocatalytic CO_2 reduction. Some optimization strategies, such as doping, have also demonstrated enhancing effect on CO_2 ECR performance using 2D metal oxide catalysts. By modifying 2D CuO with SnO_2, Lan *et al.* recently reported a high faradaic efficiency of 22% for C_2H_4 at a low over potential of −1.0 V_{RHE}.[31] The outstanding performance was attributed to the facilitated CO_2-substrate bonding on Sn modified CuO. Fig. 1c shows the morphology of the catalyst studied in the research.[31]

2.3 Two-dimensional 2D transition metal dichalcogenides (TMDs)

Transition-metal dichalcogenides (TMDs) are a promising class of two-dimensional materials which are broadly applied in electrocatalytic reactions because of their unique metal–sulfur covalent bond, atomically flat facet, and high specific surface area.[21] Notably, WS_2 and MoS_2 are two representative 2D TMDs electrocatalysts for CO_2 reduction, and the main products in such systems are CO chemicals.[62] A representative TEM image of MoS_2 nanosheet is shown in Fig. 1d.[32] To note, the use of 2D TMDs electrocatalysts, unlike other types of materials, requires an ionic liquid (1-ethyl-3-methylimidazolium tetrafluoroborate, EMIM-BF_4) in the electrolyte. The ionic liquid plays a crucial role in forming the $[EMIM\text{-}CO_2]^+$ complex in acidic environments, which could effectively suppress the HER side reaction.[62,63] Abbasi *et al.* demonstrated that metal-terminated edges in TMDs are mainly responsible for the remarkable dominated catalytic activity in CO_2 reduction due to high density of d-electrons and metallic character *via* DFT calculations. A high spin-polarized partial DOS for Mo atoms at edge sites of MoS_2 could improve the catalysis efficiency of CO_2 reduction, and the rate-determining step in CO_2 reduction is the desorption of CO* species adsorbed on edge Mo atom of MoS_2. It is found that the electron-transfer properties in 2D transition metal dichalcogenides determined the catalytic activity of CO_2 reduction.[64] Doping 5% Nb element into MoS_2 could facilitate the shift of the d-band center of edge Mo atom toward a less negative value, leading to a weakened binding of CO and 1 order improvement for CO turnover frequency. Asadi *et al.* evaluated the CO_2 electrocatalytic activities of a series of 2D TMDs, including MoS_2, WS_2, $MoSe_2$, and WSe_2 nanoflakes and revealed that the electron transfer properties of TMDs are critical in enhancing their CO_2 reduction performances.[63] With

the lowest work function among all nanoflakes prepared in this study, WSe_2 nanoflakes terminated with W atoms exhibited the excellent performance in the conversion of CO_2 into CO, showing a high current density of 18.95 mA cm^{-2}, a faradaic efficiency of 24%, and a turnover frequency of 0.28 s^{-1} for CO formation at −0.164 V (*versus* RHE).[63] Furthermore, ternary TMD alloys demonstrated enhanced CO_2 reduction performance than their binary TMD counterparts. Notably, for CO production performed at −1.15 V (*versus* RHE), MoSeS alloy monolayers displayed a higher faradaic efficiency (45.2%) for CO production than MoS_2 monolayers (16.6%) and $MoSe_2$ monolayers (30.5%), and its current density (43 mA cm^{-2}) was about 1.3 and 2.7 times higher than that of $MoSe_2$ and MoS_2 monolayers, respectively.[65] This improvement is attributed to the optimized d-band electronic structure of Mo atoms in alloys. Such optimization increases density of states near conduction band edge and improves electron transfer.[65] Theoretical calculations further illustrated that the off-center charge around Mo atoms not only better stabilized the COOH* intermediate, but also liberated the rate-limiting CO desorption step.[65] In this aspect, Nørskov and coworkers found that breaking the linear scaling relations between the binding energies of intermediates could enhance the catalytic efficiency of CO_2 reductions and promote the stabilization of intermediates, such as COOH*, CHO*, COH*, and CO*.[66] By theoretical calculations, they demonstrated that doped MoS_2 can create two binding sites, namely metal and sulfuring binding sites, and thus two different linear scaling relationships.[66] The binding of CO and CHO* on the sulfur site can form different moieties: a close-shell "SCO" moiety for CO and an open-shell "SCHO" moiety for CHO*. "SCO" moiety weakens the neighboring S–Ni bond and increases the distortion, while "SCHO" moiety showed little impact on the neighboring S–Ni interactions and minimal distortion energy. This discovery should also fit other metal/p-block materials, where two binding sites are present.

Notably, many other ultrathin two-dimensional transition metal dichalcogenides have been applied in photocatalytic CO_2 reductions, which offers an important opportunity for photoelectrocatalytic CO_2 reduction. One-unit-cell $ZnIn_2S_4$ layers with poor zinc vacancies and with rich zinc vacancies were prepared *via* hydrothermal method to study photocatalytic CO_2 reduction.[67] $ZnIn_2S_4$ with rich zinc vacancies exhibited 3.6 times higher than $ZnIn_2S_4$ with poor vacancies in formate yield, and its catalytic activity remain unchanged after 24 h photocatalysis.[67] Whereafter, atomically thin $CuIn_5S_8$ and that with sulfur deficient were synthesized to measure photocatalytic CO_2 reduction. 2D $CuIn_5S_8$ generally contained poor selectivity for CO and CH_4 from CO_2, while those with sulfur deficiencies showed higher activity and selectivity. Experimental results demonstrated that charge-enriched Cu–In dual sites in sulfur-deficient $CuIn_5S_8$ could promote the formation of stable Cu–C–O–In intermediate, which made it possess near 100% selectivity towards photocatalytic production of CH_4 from CO_2.[68] This regulation not only changed the reaction pathway to form CH_4 instead of CO in CO_2 reduction but also decreased the overall activation energy barrier in catalytic reaction. Furthermore, 2D SnS_2 nanosheets were used to study photocatalytic CO_2 reduction. Partially oxidized SnS_2 nanosheets showed excellent catalytic activity for CO production, which near 2.3 and 2.6 times higher than the poorly oxidized SnS_2 nanosheets and the SnS_2 nanosheets.[69] These works confirmed the potential application of untapped two-dimensional transition metal dichalcogenides in photoelectrocatalytic CO_2 reduction, which may also achieve high-efficiency conversion of important C_2 production.

2.4 Two-dimensional 2D carbon-based materials

Two-dimensional carbon-based materials, such as graphene and g-C_3N_4, have attracted intense attention in CO_2 reduction due to their outstanding electrical conductivity, low cost, and adjustable surface structure.[70] Despite these qualities, two-dimensional pristine graphene is relatively chemically inert, and it has a weak absorption for molecular CO_2 and poor catalytic activity for electrochemical CO_2 reduction. The well delocalized π bonding network in pristine graphene possesses a high activation energy barrier for the endothermic absorption of key intermediates (*e.g.*, COOH*, OCHO*).[71] Specifically, the undoped zigzag edge of graphene displays a relatively high energy barrier of ∼1.3 eV for CO_2 absorption in electrochemical CO_2 reductions.[72] Therefore, engineering the electronic structure of graphene is of vital importance to improve electrocatalytic activity. The enhancement approaches will be discussed in later sections.

MXenes, a category of emerging two-dimensional solid materials made up of transition metal carbides, carbonitrides, and nitrides, received much attention in the field of electrocatalysis.[73] The general formula of MXene is $M_{n+1}X_nT_x$ (n = 1, 2, 3), where M is a transition metal, X represents carbon and/or nitrogen, and T denotes the surface terminations, such as O, OH, and F.[74] MXenes layers are attached together *via* van der Waals forces. MXenes materials are generally prepared by selective etching of specific atomic layers in layered precursors (MAX phases), and their surface contains various functional group after treatment. Therefore, the surface termination in MXenes has significant impacts on the electronic and catalytic properties.[25,75] Li *et al.* first predicted the outstanding CO_2 capture capability of two-dimensional MXenes from group IV to VI series through density functional theory calculations. Furthermore, they found that the Cr_3C_2 and Mo_3C_2 MXenes possess high selectivity and activity for electrocatalytic CO_2 reduction, and these surfaces are more inclined to chemisorbing CO_2 than H_2O.[76] In the conversion process of $CO_2 \rightarrow CH_4$, the formation of $OCHO^{\bullet}$ and $HOCO^{\bullet}$ radical species is a part of the spontaneous reactions in the early hydrogenation steps, and it is considered the rate-determining step for CO_2 reduction. DFT results showed that MXenes (Cr_3C_2 and Mo_3C_2) with surface functional groups (*e.g.*, –O or –OH) can dramatically decrease the overpotentials in electrocatalytic CO_2 reduction compared to bare Cr_3C_2 and Mo_3C_2, reducing the energy input from 1.05 and 1.31 eV to 0.35 and 0.54 eV for Cr_3C_2 and Mo_3C_2, respectively.[76] Chen *et al.* systematically studied electrocatalytic activity for CO_2 reduction reaction on

17 different MXenes with –OH termination groups *via* the first-principles approach.[25] Among these catalysts, $Sc_2C(OH)_2$ and $Y_2C(OH)_2$ showed the least negative limiting potential of −0.53 and −0.61 V in catalyzing CO_2 reduction into CH_4.[25] Furthermore, they found that the adsorbed species can be better stabilized by the H atoms in $–OH^–$ terminated MXenes and that the strong –H binding can suppress the competing HER reaction. Such mechanisms can dramatically improve the activity, selectivity, and stability of electrocatalytic CO_2 reduction. Bader charge analyses confirmed that less charge migration in MXene catalysts during the potential-limiting step (*(H)COOH → *CO elementary step) can well promote the catalytic performance for CO_2RR.[25]

Handoko *et al.* also used DFT calculations to predict the property of two-dimensional MXenes in electrocatalytic CO_2 reduction, where W_2CO_2 and Ti_2CO_2 were found to be the most promising MXene catalysts with low overpotential and good selectivity for CO_2 reduction to CH_4.[77] DFT results showed that the accessible *HCOOH pathway is more favorable than the *CO route in electrocatalytic CO_2 reduction process and that the binding energies of *COOH and/or *HCOOH are the important limiting step of MXene catalysts.[77] Furthermore, their study also showed that O-termination functional groups on MXenes have vital effects on stabilizing the reaction intermediates and are the key reasons why MXenes possess good activity and high selectivity for CO_2 reduction. Soon afterwards, Xiao *et al.* also systematically investigated the CO_2 reduction reaction in 2D MXenes (M = Sc, V, Cr, Mn, Zr, Nb, Mo, Mo_2Ti, Hf, Ta, and W) *via* DFT calculations.[78] They found that the transition metal in catalysts has important effects on the active site of CO_2 reduction and that the surface bicarbonate species on MXenes can suppress HER reaction for improving the selectivity of CO_2RR. Furthermore, two possible catalytic mechanisms for CO_2 reduction into CH_4 were also proposed:[78]

Mechanism I:

$$* HCO_2 \rightarrow * H_2CO_2 \rightarrow * H_2CO_2 \rightarrow * H_2COOH \rightarrow * H_2CO \rightarrow * H_3CO \rightarrow * O \rightarrow * OH \rightarrow * H_2O$$

Mechanism II:

$$* COOH \rightarrow * HCOOH \rightarrow * CHO \rightarrow * HCHO \rightarrow * H_2COH \rightarrow * H_3COH \rightarrow * CH_3 \rightarrow * CH_4.$$

Among these MXenes, Sc_3C_2, Ta_3C_2, and Ti_3C_2 are considered efficient electrocatalysts for reducing CO_2 to CH_4. Other materials, such as Mo_3C_2, V_3C_2, Mo_2TiC_2, and W_3C_2, are predicted to possess lower overpotentials of 0.74 V, 0.45 V, 0.17 V, and 0.41 V in CO_2RR, respectively.[78] In addition, single atom catalyst systems have also been studied with MXene. Recently, single atom copper immobilized MXene $Ti_3C_2Cl_x$ demonstrated a high faradaic efficiency of 59.1% for CH_3OH.[33] X-ray absorption spectroscopy and DFT calculations revealed that single atom copper can lower the energy barrier for the conversion of HCOOH* to absorbed CHO* intermediate due to its unsaturated electronic structure. Fig. 1e shows the TEM image of the 2D MXene with copper single atom.

2.5 Metal–organic frameworks and covalent organic frameworks

Metal–organic frameworks (MOF) composed of metal and organic ligands are a class of porous, crystalline materials and have been intensively studied in various fields due to their tunable structures, vast porosity, and large surface area.[79] Notably, ultrathin 2D MOF nanosheets with larger surface area, adjustable chemical compositions and electronic structures, and more uniform pores can provide numerous surface active sites and greatly promote ion and electron transfers, making them highly suitable materials for CO_2 conversion applications.[80,81] Cui *et al.* systemically studied CO_2 reduction activity for a family of emerging two-dimensional metal–organic frameworks (MOFs) *via* density functional theory (DFT) calculations.[82] They found that Mo-based MOF exhibits good activity of CO_2 activation, and the energy barrier in Mo-based MOF for CO_2 reduced into methane is only 0.27 eV.[82] These corresponding energy inputs in CO_2 reduction are substantially lower than traditional pure metal catalysts and some single atom catalysts with noble metal. Recently, a layered, bimetallic 2D conjugated metal–organic framework (2D c-MOF) with copper-phthalocyanine as ligand (CuN_4) and zinc-bis (dihydroxy) complex (ZnO_4) as linkage (PcCu-O8-Zn) was created and exhibited a high CO selectivity of 88% with excellent durability.[83] This performance is attributed to the synergistic effects between highly efficient ZnO_4 catalysts and CuN_4 centers. This study reveals the feasibility and advantages of utilizing bimetallic MOF catalysts. Similar to MOFs, 2D covalent organic frameworks have also exhibited outstanding CO_2 reduction efficiency and selectivity. Lin *et al.* developed covalent organic frameworks (COFs) composed of cobalt porphyrin catalysts linked by organic struts and demonstrated the advantages of such materials in catalytic CO_2 reduction.[84] As a result of the π conjugation and π–π stacking in the COF, the charge-carrier mobility is significantly improved, resulting in a high FE_{co} of 90% and a turnover number of up to 290 000 at −0.67 V *vs.* RHE, demonstrating a 26-time increase in activity compared with molecular cobalt complex.[84] In addition, other 2D electrocatalysts can also be derived from metal organic frameworks and used for CO_2 ECR applications. For instance, 2D bismuthine has been derived from a Bi-based metal organic framework and demonstrated a high faradaic efficiency of more than 96% for formate production with large current densities and stability.[34] Fig. 1f and g show the morphologies of such MOF-derived structures. This example has provided novel approaches to utilize MOF in the field of CO_2 ECR.

3 Regulating strategies for 2D electrocatalysts for CO_2 reduction reaction

Many advanced strategies have been introduced to improve the CO_2 electrocatalytic performance of two-dimensional materials

by increasing the number of active sites and enhancing the activities of active sites. Generally, common approaches include structure and phases engineering, defect engineering, and nano composites.[85,86] The desired outcomes of such optimizations are (1) higher current density at low overpotentials towards high-value products, (2) greater selectivity in single products and inhibiting the competitor HER reaction, and (3) enhancing long-term durability in catalytic processes.[3] This section will review some advanced strategies to optimize 2D solid catalysts for CO_2 electrocatalytic reductions.

3.1 Structure engineering

Surface functionalization in solid catalysts is one of the most powerful methods to directly influence catalytic properties *via* modulating the electric and absorption properties of material surfaces. A recent study by Cheng *et al.* used a surface nitrogen-injection approach to reach high activity and selectivity for CO_2 conversion into formate. The nitrogen abundant Sn nanosheets (N–Sn) showed a 5-times higher current density and a 2.45-times higher faradaic efficiency than that of pristine 2D Sn nanosheets, resulting in a high productivity of 1358 μmol h^{-1} cm^{-2}.[27] The nitrogen abundant Sn surface has a higher CO_2 adsorption capacity than pristine Sn surface, because of the coordination between Sn and N atoms. Additionally, the undercoordinated Sn and defect sites created a higher active surface area of 90.79 mF cm^{-2} in N–Sn, much higher than the 64.18 mF cm^{-2} found in pristine S nanosheets.[27] DFT calculations revealed that the valence electrons of S atoms were increased from 6 to 6.86, suggesting a more positively charged $Sn^{\delta+}$ in N–Sn samples that resulted in higher reaction activity and selectivity.[27]

Surface defect engineering has been a hot research topic in heterogeneous catalysis. Current research suggests that the abundant oxygen vacancies in 2D transition metal oxides, such as Co_3O_4 and Bi_2O_3, can promote the CO_2 adsorption on catalyst surface and accelerate the desorption of products from surface, thus reducing the rate-limiting activation energy and improves the activity and durability in CO_2 reduction reaction.[87,88] A recent study on oxygen defective Bi_2O_3 nanosheets revealed that oxygen vacancies can result in a negative adsorption energy of −0.3 eV on the catalyst surface and promote the generation of $CO_2^{\bullet-}$ radicals *via* a single-electron transfer process.[88] The oxygen defective Bi_2O_3 demonstrated localized electrons around the oxygen vacancies, thus enhancing the interactions with CO_2 on catalyst surface.[88] The impacts of oxygen vacancies on CO_2 ECR performance were also investigated with Co_3O_4 atomic layers. It was discovered that the oxygen(II) vacancy decreased the activation barrier by stabilizing the $HCOO^{-}$* intermediates and promoting the proton transfer. Consequently, a high formate selectivity of 85% was achieved in vacancy rich 2D nanocatalyst.[87]

Furthermore, rich cationic vacancies and sulfur vacancies can promote the formation of the intermediate in CO_2 reduction using 2D nanocatalysts, leading to improved selectivity, activity, and stability of CO_2 reduction. Peng *et al.* reported the enhanced CO_2 ECR to *n*-propanol using CuS 2D catalysts with double sulfur vacancies.[89] It was discovered that the highly dense double sulfur vacancies in copper sulfide (100) planes can act as electrocatalytic centers to stabilize CO* and OCCO* dimers and promote the CO–OCCO coupling to yield C_3 products. This phenomenon was not observed in CuS with single or no sulfur vacancies. Consequently, a high faradaic efficiency of 15.4% for *n*-propanol was observed.[89] In addition, some other research showed that defect engineering in graphene is of vital importance for tuning the electronic structure and catalytic performance.[90,91]

The morphologies of 2D materials can play an important role in determining the CO_2 ECR performance. Structure engineering can significantly enhance CO_2 ECR performance by modulating the number of exposed active sites and affecting the chemisorption. Using a halogen-assisted calcination approach, Shu *et al.* synthesized 2D nitrogen-doped carbon from ZIF-8 precursor with a large electrochemical surface area of 788 to 1413 m^2 and a high G–N ratio of 42.27 to 55.06%.[92] When the surface area increased from 788 m^2 g^{-1} in the N/C-1100 sample to 1413 m^2 g^{-1} in the N/C–Cl-1100 sample, the resulted current density showed a pronounce improvement, and the CO selectivity increased from 91.2% at −0.7 V to 99.5% at −0.5V.[92] Fig. 2a shows the FE of catalysts with different surface areas. Additionally, the highest G–N ratio was also found in the N/C–Cl-1100 sample, suggesting a high active sites exposure. It was proven in this study that the increased G–N exposure can significantly promote the CO_2 electrochemical conversion to CO. This significant enhancement demonstrated the effect of surface area and active site exposure on the catalytic performance in 2D materials.

Modulating the exposure of active edges sites is another effective approach to enhance CO_2 ECR performance. DFT calculations have suggested that edge sites are highly active catalytic sites for CO_2 ECR using nanoparticles, calling for tunable 2D structures with high edges-to-corner site ratios.[93] Layered 2D structures have demonstrated superior performance to their bulk counterparts in CO_2 ECR, due to the exposure of more edges and defects for catalytic reactions.[85,94] Recently, Li *et al.* synthesized layered Sb nanosheets by cathodically exfoliating bulk Sb crystals and demonstrated enhanced CO_2 ECR to formate performance.[94] With the same layer thickness, smaller Sb nanosheets with an average lateral size of 170 nm showed a 3.6-times higher peak current (mass loading normalized) than showed in larger Sb nanosheets with an average lateral size of 485 nm at a potential of −0.96 V, resulting in a FE of 84% for formate at −1.06 V.[94] The morphology-dependent CO_2 ECR performance of nanoplates was also observed with triangular silver nanoplates. Liu and coworkers discovered that Ag nanoplates demonstrated higher faradaic efficiency and energy efficiency than their Ag nanoparticle counterparts with similar sizes.[93] This enhancement was attributed to the larger amount of edge sites and higher edge-to-corner ratios in nanosheets, as the adsorption of CO_2 and the formation of COOH* are more promoted on edge sites.[93]

The exposure of different facets is also a critical parameter in CO_2 ECR that determines the CO_2 ECR efficiency and

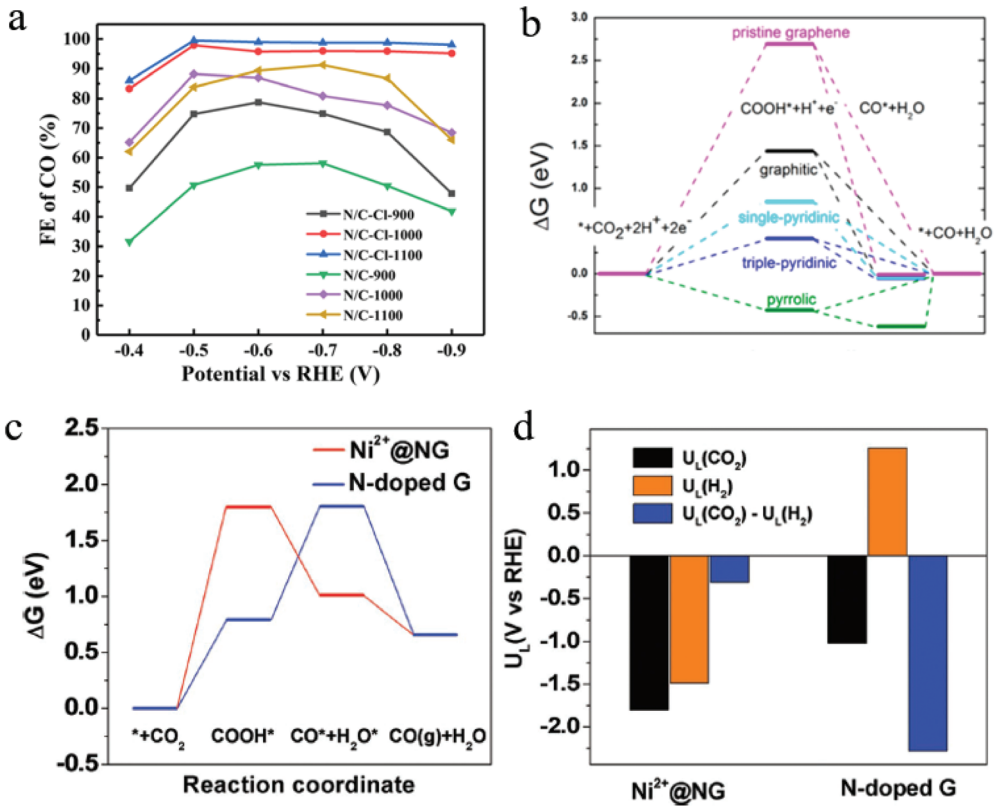

Fig. 2 (a) FE of catalysts with different surface areas. Copyright 2021, Springer Nature; (b) free energy diagram of CO_2 ECR to CO on different NG surfaces. Copyright 2016, American Chemical Society; (c) free energy diagrams and (d) the calculated limiting potentials for CO_2RR and HER on composite and pristine graphene surfaces. Copyright 2018, John Wiley and Sons. All panels reproduced with permission.[23,92,96]

selectivity. Surface reconstruction has become an effective approach to program the desired exposure of facets, thus enhancing the CO_2 ECR of 2D materials. A recent work demonstrated that the preferred exposure of Bi $(1\bar{1}0)$ facets causes an increased FE of 90% for formate at a high current density of 200 mA cm^{-2}, due to the lower reaction energy barrier (0.03 eV) for CO_2 ECR exhibited on the Bi $(1\bar{1}0)$ facet than the energy barrier (0.74 eV) on the Bi (121) facet.[26] Moreover, the stepped Bi $(1\bar{1}0)$ surface also showed a Gibbs free binding energy of −0.01 eV for HCOO*.[26] This value is very close to the thermodynamic minimum. The facet-dependent performance was also observed in other nanosheets. For Ag nanoplates, the Gibbs free energy (ΔG) for forming COOH* was found to be lower on Ag (100) than on Ag (111), making Ag (100) the preferred facet for CO_2 ECR using nanoplates.[95]

In 2D materials, doping is an extremely effective approach to tune the catalytic performance. Unlike in bulk materials, where dopants are located within the materials, doped 2D materials have more dopants exposed on the surface that can affect the overall catalytic performance. Nitrogen doping is a successful approach to enhance the CO_2 ECR performance using 2D carbon materials. In a recent study, three types of N dopants on graphene were prepared and investigated by Wu *et al.*: graphitic N, pyridinic N, and pyrrolic N, where the lowest uphill free energy barrier of COOH* adsorption was observed in samples with triple-pyridinic N dopants.[96] Fig. 2b shows the free energy diagram of CO_2 ECR to CO on different graphenes. It was found that the positively charge C atoms adjacent to N dopants are the active sites for CO_2 ECR. Additionally, DFT calculations suggested that N doping can significantly reduce the energy barrier for COOH* adsorption, and the direct protonation of COOH* requires significantly lower energy barrier (−0.5 eV) to form CO gas and H_2O than that needed for the Heyrovski step to form H_2 (−2.0 eV).[96] Thus, this doping approach can greatly promote the CO formation and inhibit the competing HER. Besides, through computational approaches, Liu and coworkers discovered that pyrrolic-nitrogen doped graphene showed a lowest theoretical over potential of 0.24 V for CO_2 ECR to HCOOH among all N-doped graphene.[97] This result suggests that pyrrolic-nitrogen doping is a promising approach for CO_2 ECR to formate. However, the role of active site in N-doped graphene materials is still controversial in CO_2 electrochemical reduction reactions. Chai and Guo found that the graphic N is the effective active site in electrochemical CO_2 reduction and has a lower activation barrier (0.58 eV).[72] Furthermore, Sreekanth *et al.* also studied CO_2 electrochemical reduction of the B-doped graphene in aqueous 0.1 M $KHCO_3$ solutions.[98] Their research results showed that boron dopants changed asymmetric charge and spin density distribution of pristine graphene, and

B/C atoms with positive spin density in graphene are important active sites.[98]

3.2 Composite materials and alloys

Engineered composite materials with heterostructures can often achieved enhanced CO_2 ECR performance by promoting charge transfer and the coupling effects between different phases. The general regulation parameters mainly involve compositions and alloys. Loading metals/metal oxides on two-dimensional graphene is a very common method to improve the electrical conductivity of metal oxides and increase the active sites of graphene. Bi *et al.* reported that the surface immobilization of Ni on nitrogen-dope graphene (Ni^{2+}@NG) demonstrated significantly improved CO_2 ECR performance with a high current density of 30 mA cm^{-2}, compared with that of pristine N-doped graphene (<10 mA cm^{-2}).[23] The FE for CO also experienced a drastic increase from below 60% to 92% in Ni^{2+} @NG.[23] By comparing the free energy barrier for the formation of *COOH, *CO, and *H, the authors found out that Ni^{2+}@NG showed a lower free energy barrier for the formation of adsorbed *CO than N-doped graphene did. Besides, compared with its pristine counterpart, Ni^{2+}@NG composite 2D catalysts exhibited a higher preference towards CO_2RR over HER, as suggested by the limiting potential calculations. Fig. 2c and 1d show free energy diagrams on different graphene surfaces and the calculated limiting potentials for CO_2RR and HER, respectively.

Loading isolated metal atoms on graphene is an emerging regulation strategy in heterogeneous catalysis.[99] These composite graphene materials have demonstrate superior CO_2RR performance due to their high electrical conductivity, abundant active sites, and maximum atom efficiency. This strategy is regarded as one of the most effective strategies for improving the activity, stability, and selectivity in electrochemical CO_2 reduction. Combined with the attributes of single-atom catalysts and 2D materials, some researchers also synthesized an atomically dispersed Fe on nitrogen-doped graphene (Fe/NG), where graphene oxide (GO) absorbed iron ions (a mixture of GO and $FeCl_3$) is annealed in an atmosphere for Ar/NH_3 at 700–800 °C.[100] Fe/NG catalyst had a large number of nitrogen-confined atomic Fe moieties on the surface as active sites, resulting in a high faradaic efficiency of ~80% for CO production at −0.60 V *versus* RHE.[100] Theoretical calculations and experimental results suggested that the isolated Fe–N_4 moiety in nitrogen-doped graphene as the activity center that enhanced CO_2 adsorption and improved CO_2 activation. Based on these works, a heterogeneous molecular Co electrocatalyst (NapCo@SNG) was prepared by immobilizing planar CoII-2,3-naphthalocyanine complexes (NapCo) on S/N/O heteroatoms doped graphene (SNG) through axial coordination.[101] Sulfoxide dopants in NapCo@SNG can enhance the electron transfer between NapCo and doped graphene, causing an increase of ~3 times in the turnover frequency of Co sites when compared with carboxyl-NapCo moiety and a high faradaic efficiency for CO production of ~97% at −0.8 V *versus* RHE.[101] In addition, Cu/N-doped graphene composite materials (p-NG/Cu) were introduced by combining monodisperse Cu nanoparticles and pyridinic-N rich graphene (p-NG).[102] The p-NG catalyst demonstrated the reduction activity and selectivity to ethylene compared with Cu and p-NG, with a faradaic efficiency of ~19% for C_2H_4 production and a 79% ethylene selectivity at ~0.9 V *versus* RHE.[102] The interaction between p-NG and ~7 nm Cu NPs facilitated CO_2 reduction, hydrogenation, and C–C coupling in the formation process of C_2H_4.

Monolayer ternary transition metal dichalcogenide (TMD) alloys have demonstrated enhanced CO_2 ECR performance compared with binary TMDs. Xu *et al.* synthesized MoSeS alloy monolayers with shortened Mo–S and extended Mo–Se bonds that can tune the d-band electronic structure of Mo atom.[65] By engineering the band structure in this way, the density of states around the conduction band edge showed a drastic increase, resulting in faster electron transfers due to the lowered work function (4.24 eV) and decreased charge-transfer resistance.[65] Moreover, the overlap between the d-orbitals of Mo and the p-orbitals of Se atoms was reduced by the off-center charge density. DFT calculations revealed that the biased electron density around Mo atom in alloy monolayers can help stabilize COOH* intermediates and facilitate the CO desorption. Consequently, at an overpotential of −1.15 V *vs.* RHE, a high current density of 43 mA cm^{-2} and a high faradaic efficiency of 45.2% for CO were observed in ternary TMD alloy monolayers.[65] Nevertheless, the low FE still needs to be improved, and the overpotential needs to be lowered to inhibit the competing HER.

4 Electrolyzers for electrocatalytic CO_2 reductions

Electrolyzers also play a decisive role in determining the CO_2 reduction performance of 2D materials. So far, various electrolyzer configurations have been developed and utilized in CO_2 ECR applications. The H-type cell, a simple configuration that employs an ion-exchange membrane to separate anodic and cathodic reactions, has been a popular electrolyzer configuration for 2D catalyst development and screening.[26,89,103,104] Catalysts can be deposited on carbon paper to form the cathode for CO_2 ECR, and the reaction products are collected directly from the cells to evaluate CO_2 ECR performance. Nevertheless, the use of H-cells is greatly limited by their low current densities (<100 mA cm^{-2}) because of the low solubility of CO_2 in liquid electrolytes.[105] In order to solve this issue, liquid-phase flow cells have been developed to directly use CO_2 gas as the CO_2 source in CO_2 ECR. Gas diffusion electrodes are applied in this configuration to allow for gas-phase CO_2 diffusions through the porous electrode and reactions taking place on the catalyst–electrolyte interface.[106] Ion exchange membranes, *i.e.*, anion exchange membrane, cation exchange membrane, and bipolar membrane, are utilized to separate the anodic and cathodic chambers. Improved CO_2 ECR stabilities, current densities, and faradaic efficiencies have been widely

reported with the use of flow cells.[105,107] In addition, modified H-cell and flow cell configurations are the most common reaction cells for *in situ* and *operando* investigations.[27,28,108,109] On the other hand, the membrane electrode assembly (MEA) is a novel gas-phase electrolyzer that uses a solid polymer electrolyte to separate the anode and cathode. The catalyst on the gas diffusion electrode is directly pressed against the membrane to form the "zero-gap" configuration that reduces the ohmic losses and maximizes the energetic efficiency.[110] Consequently, high current densities (>1 A cm^{-2}) and faradaic efficiencies have been reported using MEA.[111–113] However, the operation of gap-phase reactors requires humidity that can be provided either by liquid electrolytes in the anode and/or humidified gas.[105] The separation of CO_2 ECR products from liquid electrolytes can be eliminated using all-solid-state electrolyzers, which adopt solid electrolytes to facilitate the continuous production of pure liquid products.[114] Remarkably, highly concentrated (~98 wt%) formic acid and acetic acid have been produced with this solid-state electrolyzers.[115,116] It can be projected that the developments and optimizations of novel electrolyzers can enhance the CO_2 ECR performance of 2D materials and facilitate *in situ* and *operando* studies to better understand reaction mechanisms.

5 Advanced *in situ* and *operando* characterization technology

During CO_2 reduction reactions, catalysts are in metastable states and subjected to constant changes in their chemical and structural properties in a complex reaction environment. Such changes include surface reconstruction, catalysts deactivation, agglomeration, phase segregation, metal reconstruction, and vacancies formation.[117–123] Many reaction intermediates are formed and consumed during the CO_2RR process to yield various final products *via* different pathways.[28] On the other hand, the changes in catalysts' chemical and structural properties can affect their catalytic performance, determining their effectivity and selectivity.[124] As illustrated in Fig. 3,[29] the elementary transferring of electrons and protons, the adsorption and desorption of intermediates and products, the mass transfer of molecules in the reaction environment, and other processes in catalytic reactions, all take place in different time and length scales. It is critical to study all such processes in a time resolved manner to gain insightful information about CO_2 catalysis. Nowadays, thanks to the developments of highly advanced *in situ* and *operando* characterization methods, fundamental studies of CO_2RR at various time and length scales have become feasible. *In situ* characterizations refer to the characterizations of catalysts under conditions relevant to catalytic operation conditions. Such characterizations might not be simultaneous to reactions. However, *operando* characterizations are simultaneous characterizations of working catalysts during real catalytic reactions.[125,126] In this section, state-of-the-art *in situ* and *operando* spectroscopy and microscopy methods are reviewed, and future research trends are proposed with the goal of achieving better understandings the mechanism and design guidelines of 2D materials in CO_2RR. We summarized the spatial and temporal resolutions of these advanced characterization techniques in Table 1.

5.1 *In situ* scanning probe microscopy

5.1.1 *In situ* scanning electrochemical microscopy (SECM). Scanning electrochemical microscopy is a type of scanning probe microscopy that utilizes an ultramicroelectrode (UME) or a nanoelectrode (NE) to probe the local current in the vicinity of a spot of interest, thus detecting the chemical species in this area.[127] This technique has been employed in CO_2RR studies to investigate the formation of different products and intermediates.[128–132] Typically, the SECM system consists of an electrochemical cell with two working electrodes: working electrode 1 being the catalyst material, working electrode 2 being

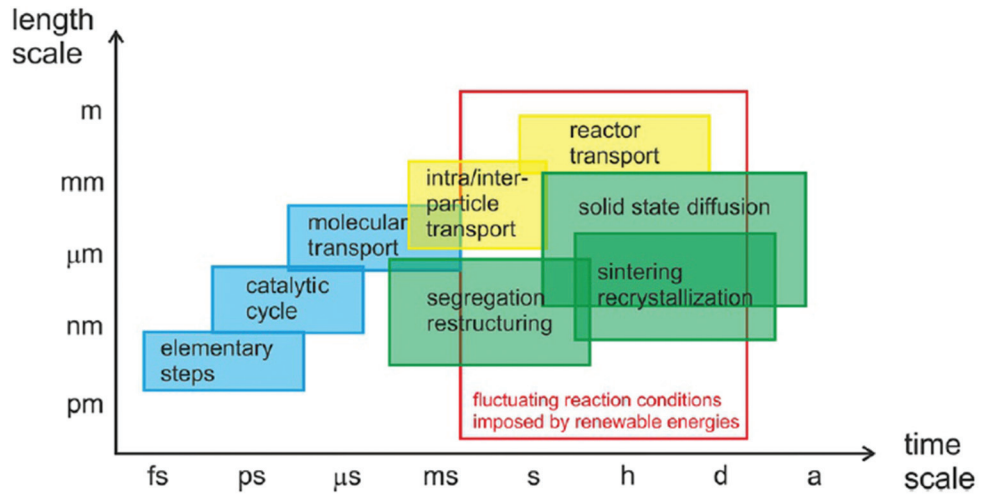

Fig. 3 Time scale of various processes in catalytic reactions. All panels reproduced with permission.[29] Copyright 2017, John Wiley and Sons.

Table 1 Temporal and spatial resolutions of *in situ* and *operando* characterization techniques

	Infrared	Raman	Synchrotron X-Ray	FEL X-Ray	Mass spectroscopy
***In situ* and *operando* spectroscopy**					
Temporal resolution	<1 ms	<1 ms	<1 ns	<10 fs	s
Spatial resolution	1 μm	1 μm	<15 nm	<15 nm	>20 μm

	TEM	SECM	STM	AFM	STXM	CDI
***In situ* and *operando* microscopy and imaging**						
Temporal resolution	200 fs	100 μs	1 μs	100 μs	<30 ps	10 fs
Spatial resolution	<0.1 nm	50 nm	1 nm	1 nm	7 nm	10 nm 10^{-4} strain

the ultramicroelectrode as the probe. The scanning and mapping of faradaic current profile of the substrate can be obtained to analyze the chemical, electrochemical, and/or topographic characteristics of the local reaction environment.[127] Fig. 4a and b illustrate the *in situ* operation mechanism of SECM in a CO_2RR environment using the substrate generation/tip collection mode (SG/TC).[128] In this example, the detection of formate product during CO_2 ECR was achieved to monitor the real time degradation of the catalytic activity and to compare the performance among catalysts of different compositional and morphological properties.

In another CO_2 ECR study, Kim *et al.* employed SECM to monitor the CO_2 ECR performance of Au nanoparticles and discovered a high selectivity of CO production without the interference of HER at low overpotentials.[133] Likewise, the time-resolved quantitative probing of CO_2RR products has also been demonstrated by Shaughnessy *et al.*, who utilized SECM in the Substrate Generation-Tip Collection mode to investigate the potential dependent CO production of a In^0–In_2O_3 composite catalyst.[130] Also, Sreekanth *et al.* employed SECM to detect the CO selectivity of Au catalyst of different surface roughness in different pH environment.[129,134] Due to its time-resolved detection ability, SECM was used in TG/SC mode to quantitatively probe the unstable, short-lived $CO_2^{\bullet-}$ intermediate in CO_2 ECR for the first time. Such intermediates have a high dimerization rate of 6.0×10^8 M^{-1} s^{-1}, a short half-life of around 10 ns, and are critical intermediates in CO_2RR. The successful monitoring of these intermediates can greatly benefit the studies of fundamental CO_2RR mechanisms.[131] However, the spatial resolution of this noncontact technique is restricted by the mass transport of products from the sample surface to the probe tip, and therefore the probe size and probe-sample distance are the main limiting factors of *in situ* ECM.[135] Besides, the SG/TC model is also limited by low collection efficiency and interferences between the sample and probe tip.[136]

5.1.2 *In situ* scanning tunneling microscopy (STM). Both *in situ* STM and AFM are capable of probing the surface structures of catalysts in a reaction environment. Electrochemical scanning tunneling microscopy (ECSTM), in particular, is suitable for surface structure investigations at the atomic and molecular level in aqueous environment and under atmospheric pressures.[137,138] Such advantages make ECSTM suitable for the studies of CO_2 ECR using 2D materials. Based on the quantum tunneling effect, STM utilizes an ultrasharp metal tip to measure the tunneling current generated when the tip is placed close to a surface. Similar to SECM, the ECSTM is also constructed with a four-electrode electrochemical bipotentiostat, which allows for the simultaneous operations of two working electrodes: working electrode 1 measures the electrochemical currents, and working electrode 2 probes the tunnelling currents.[139] Fig. 5a illustrates the principle of *in situ* ECSTM. Using this technique, Tsang *et al.* monitored the potential-dependent surface reconstruction behaviors of polycrystalline Cu at a CO_2RR potential. They used the *in situ* STM

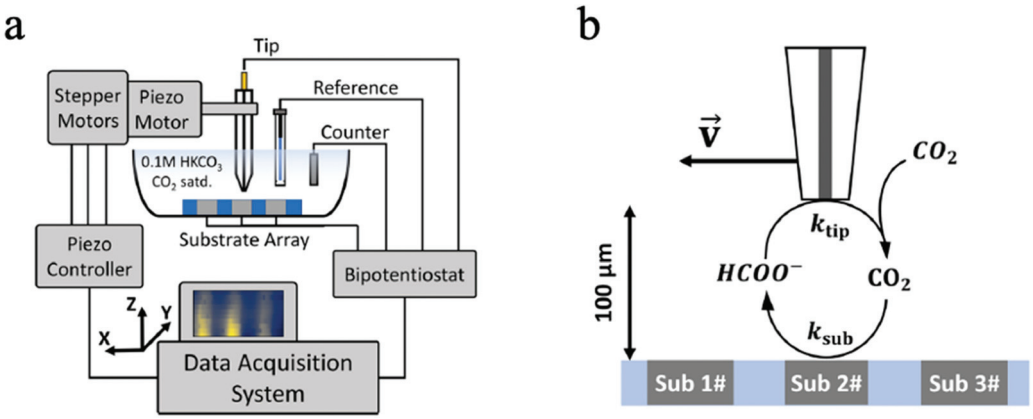

Fig. 4 (a) SECM operation principle; (b) the SG/TC mode all panels reproduced with permission.[128] Copyright 2020, Springer Nature.

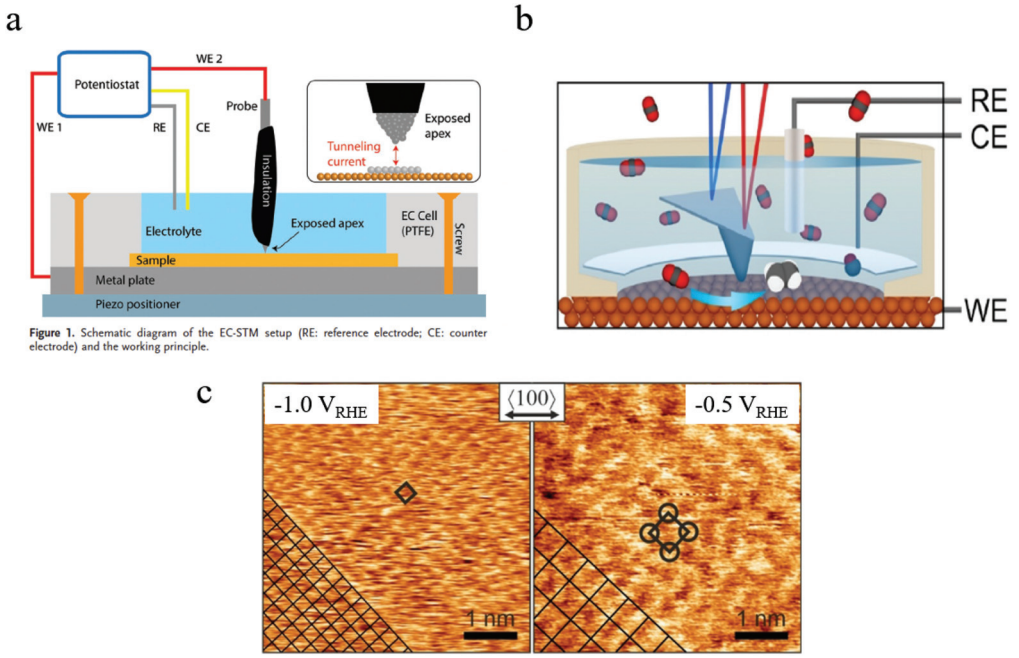

Figure 1. Schematic diagram of the EC-STM setup (RE: reference electrode; CE: counter electrode) and the working principle.

Fig. 5 (a) Schematic of *in situ* EC-STM setup. Copyright 2018, John Wiley and Sons; (b) schematic of *in situ* EC-AFM; (c) morphology of Cu surface at different potentials characterized by *in situ* AFM. Copyright 2020, John Wiley and Sons. All panels reproduced with permission.[139,143]

to monitor the construction of Cu (100) and Cu (511) facets at different potentials and prepared oxide-free Cu (511) structures.[140] With additional quartz-crystal nanobalance and differential electrochemical mass spectrometry characterizations, the authors investigated the CO adsorption behaviors and proved that effective CO dimerization can only occur after a certain degree of CO coverage on the catalyst surface, leading to the formation of CH_3CH_2OH.[140] The same group of researchers also reported the cathodic regeneration of Cu (100) from air-oxidated surfaces under a typical CO_2RR condition.[141] Additionally, they revealed the evolution of polycrystalline Cu to Cu (111) after 30 min of experiment in a 0.1 M KOH solution, at a CO_2RR potential of −0.9V.[141] Interestingly, after another 30 min, Cu (111) further transformed into Cu (100). By adopting such time resolved monitoring of Cu surface, researchers hope to construct the "structure–composition–reactivity correlations" of heterogeneous electrocatalysts.[142]

5.1.3 *In situ* atomic force microscopy (AFM). Electrochemical Atomic Force Microscopy (EC-AFM) is another powerful scanning probe microscopy that is capable of investigating the catalyst surface morphology and surface potentials in *in situ* CO_2 ECR studies. A typical EC-AFM setup consists of a three-electrode electrochemical cell and an AFM with its tip submerging in the liquid electrolyte. For morphological studies, the amplitude modulation mode (AM-AFM) can be used to scan the surface of catalysts during reactions.[143] Fig. 5b illustrates the mechanism of this *in situ* measurement technique. On the other hand, the measurement of catalyst surface potentials involves a conductive AFM tip that directly contacts the sample and measures the catalyst surface potentials.[144] Using *in situ* EC-AFM, Grosse and coworkers observed the change in Cu nanoparticles during a CO_2 ECR process. During the experiment, they observed drastic structural changes in Cu nanocubes. The loss in sharp corners and edges was observed after 1 min of CO_2 ECR process, and a 10% decrease in the particle size was probed after 3 hours.[145] Later, a correlation between such changes and the CO_2 ECR FE and selectivity was constructed. Smaller 220 nm-cubes were found to be more prone to morphological changes, leading to a drastic decrease in EF and an increase in selectivity towards C_1 products.[145] Recently, Simon *et al.* investigated the potential-dependent changes in the morphology of Cu catalyst in CO_2 ECR.[143] They found that at a low potential of −0.5 V (RHE), the Cu (100) electrode surface exhibited round, smooth island and terrace structures. At −1 V (RHE), rectangular islands with step edges replaced round islands, indicating the formation of low-coordination sites. However, at −1.1 V (RHE), the size of rectangular structures reduced due to cathodic corrosion. Moreover, with the help of atomically resolved *in situ* imaging, the morphological change due to surface absorption was also detected with a $p(2 \times 2)$ superstructure present at −0.5 V (RHE) and a (1×1) surface termination at −0.1 V (RHE).[143] Fig. 5c shows the morphology of Cu surface at these two potentials. This work exhibited the outstanding *in situ* measuring capability of EC-AFM with an atomic resolution.

5.2 *In situ* and *operando* microscopy and imaging

5.2.1 *In situ* and *operando* transmission electron microscopy (TEM). *In situ* and *operando* TEM can provide real time observations of the morphological properties of solid,

gaseous, and liquid reactants and catalysts with high spatial resolutions. It is a versatile technique that can be employed to study both liquid phase and gas phase reaction environment at atmospheric pressure, which can reflect the realistic working conditions for most of catalytic reactions.[146–148] A high vacuum environment is usually maintained in the traditional TEM. However, *in situ* and *operando* studies require a real reaction environment around the sample. To meet this requirement, two methods have been developed to introduce gas and/or liquid to the reaction environment: (1). modified TEM. With Environmental Transmission Microscopy (ETEM), gas can be introduced to the sample using a differential pumping mechanism, which employs a set of differential apertures to control different pumping and pressure conditions inside the TEM. Consequently, a higher pressure at the sample area (~a few millibars) can be achieved with the introduction of reactant gas, while the rest of the ETEM column is still maintained at a high vacuum.[147,149,150] (2). Modified sample holder. In this approach, the sample and reaction environment are kept within a sealed micro device, which is inserted to the TEM column to encapsulate the reaction environment while maintaining a high vacuum in the TEM column.[146–148] Electron-transparent windows, usually made of silicon nitride membranes, are used above and under the sample for electrons to transmit.[151] Notably, advanced micro devices can be fabricated by integrating a micro electrochemistry cell and a TEM sample holder, enabling electrochemical reactions to take place and be characterized inside the *in situ* TEM.[146,152] This application is particularly helpful in electrochemical CO_2RR studies using 2D materials. Fig. 6a illustrates the mechanisms of crystal growth in an electrochemical cell using *in situ* and *operando* TEM characterization approaches.[152]

Benefited from *operando* TEM technology, our group studied the facet-dependent CO_2 catalytic reduction behaviors of Cu_2O nanoparticles and discovered that the (110) facet of Cu_2O nanoparticles is catalytically active in CO_2RR, while the (100) facet is not active.[148] The *operando* TEM was used to identify nanoparticles and facets of interest and guided the use of focused electron beam and nano-focused synchrotron X-ray beams to desired facets for localized spectroscopic investigations using electron energy loss spectroscopy (EELS) and X ray absorption spectroscopy (XAS).[148] In a recent publication by Wang *et al.*, a micro electrochemical cell ("*in situ* TEM E-chip cell") was employed to investigate the real-time morphological changes in 2D CuO nanosheets in a CO_2 ECR environment.[153] They discovered the potential- and time-dependent conversions of 2D CuO nanosheets into nanoscale fragments, which consecutively agglomerate and form Cu dendrites. The formation of undercoordinated Cu sites was found to promote the CO_2 electrochemical conversions into C_{2+} products. This *operando* TEM successfully revealed the operation condition–morphology-performance relationship of CO_2 ECR using CuO nanosheets as the catalyst. Additionally, Vavra and coworkers recently monitored the dissolution/redeposition of Cu nanocatalyst in CO_2 ECR.[154] They found that, at the open circuit voltage, the oxidation and the dissolution of Cu nanoparticles took place at the same time, yielding Cu_2O and dissolved Cu ions in the initial electrolyte. Later, at higher catho-

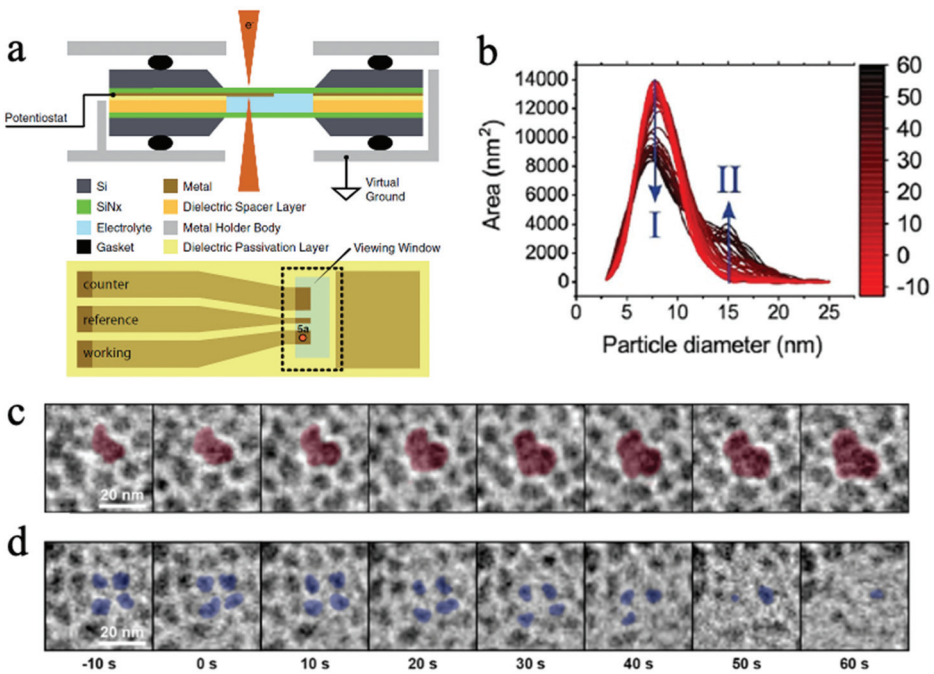

Fig. 6 (a) The schematic of a micro electrochemical cell for *in situ* TEM. Copyright 2017, IOP Publishing, Inc.; (b) the change in primary (I) and secondary (II) particle sizes as experiment progresses; (c) the growth of secondary particles, and (d) the shrinkage of primary particles. Copyright 2020, John Wiley and Sons. All panels reproduced with permission.[152,154]

dic potentials, the dissolved Cu^{+} and Cu^{2+} ions are reduced back to solid Cu phase, generating larger secondary Cu nanoparticles. It was also proposed that the Cu surface oxide, Cu_2O, participated in the reconstruction process of Cu nanocatalyst as the CO_2 ECR experiment progressed.[154] With the help of time resolved monitoring at the nanoscale, the catalyst phase change mechanisms were investigated. Fig. 6b depicts the change in primary and secondary particles. Fig. 6c and d show the *in situ* observation of the morphological change in primary and secondary particles.

Nevertheless, there are still some limitations in such *in situ* and *operando* TEM characterizations. For example, it is still challenging to get high-quality 3D reconstructed images using *in situ* and *operando* TEM. One reason is due to the limited tilting angles inside TEM if using electrochemical cell. The gas bubbles generated in CO_2RR might affect the local reaction environment, and this impact is much amplified in the micro reaction system where only a small amount of electrolyte is present.[124] Additionally, the CO_2 saturation in electrolyte results in deteriorated resolution and lowered contrast, due to inelastic electron scattering in liquids.[154] It was also reported in the same publication that a high electron dose can damage the catalysts within a short amount of time. Hence, the electron dose needs to be fine-tuned to avoid damaging the catalysts while achieving an optimal resolution.

5.2.2 *In situ* and *operando* scanning transmission X-ray microscopy (STXM). Synchrotron-based *in situ* Scanning Transmission X-ray Microscopy (STXM) is a powerful tool to characterize active electrochemical cells by providing high spatial and temporal resolution images and spectra with excellent chemical, electronic, and bond orientation contrasts.[155] In STXM, synchrotron and undulator-generated monochromatic X-rays first pass through a zone plate that focuses X-rays onto the sample plane, and the sample is raster-scanned by the focused X-rays. Then, the transmitted X-rays are measured by detectors to construct images. With an additional fluorescence detector installed, Scanning X-Ray Fluorescence Microscopy (SXFM) can be combined with STXM to detect the fluorescent photons and reveal the distributions of elements on samples with unparalleled sensitivity.[156] Also, the X-ray absorption properties of materials can provide chemical bonding information and elemental composition information with high chemical contrast.[157] Fig. 7a illustrates the setup of STXM and SXFM. Advanced zone plate lenses and setups have enabled STXM to reach a spatial resolution of 7 nm and a temporal scanning resolution of 20–30 ps.[158,159] The spectral resolution of soft X-rays at some synchrotron facilities can be as high as 0.1 eV.[157] By adopting an electrochemical nanoreactor, *in situ* and *operando* STXM characterizations of working electrocatalysts can be conducted at atmospheric pressure and up to 350 °C.[160] STXM images and spectra can probe critical information about catalytic reactions, including catalysts morphologies, the changes of catalyst phases and chemical states, as well as the properties and locations of catalytic reactants.[160,161] In a recent study conducted by our group, *operando* SXFM was employed to conduct imaging and nanospectroscopic investigations of Cu_2O nanocatalysts for CO_2 reductions. The location and morphology of a single Cu_2O nanoparticle of interest were determined by low-resolution and high-resolution SFXM images, respectively. The corner of the particle was revealed to be the (110) facet, while the edge is the (100) facet. By directing the nanofocused X-ray beam paral-

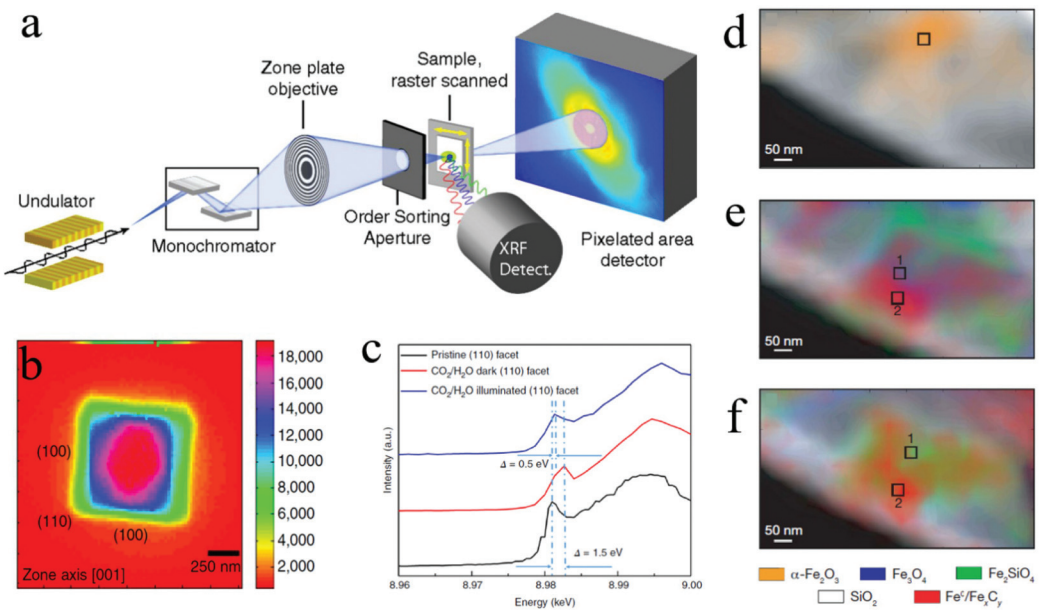

Fig. 7 (a) STXM and SFXM setup; Copyright 2014, National Academy of Sciences; (b) SFXM image of a Cu_2O nanoparticle; (c) scanning X-ray nanospectroscopy of the (110) facet; Copyright 2019, Springer Nature; (d) to (f) chemical contour images of the catalyst under different treatments; Copyright 2008, Springer Nature. All panels reproduced with permission.[148,156,160]

lel to different facets, the facet-dependent X-ray fluorescence spectra were obtained to evaluable the active sites during CO_2 reduction reactions. The shift observed in the spectra generated on the (110) facet under reaction conditions revealed that the (110) facet is active for CO_2 reduction.[148] Fig. 7b and c are the high-resolution image of a Cu_2O nanoparticle with facets identified and the scanning X-ray nanospectroscopy of the (110) facet under different conditions. Our group also utilized an electrochemical liquid cell with STXM and XAS to characterize the non-dissolution nature of electrodeposited species on electrodes. It was observed that the non-dissolvable Mg thin film during discharging was hexacoordinated Mg compounds.[146] This example is particularly relevant to 2D materials for CO_2 ECR applications, as similar *in situ* and *operando* techniques can be applied to investigate the surface reconstruction phenomenon of 2D catalysts during reactions. A study by Smith *et al.* demonstrated the capability of STXM to examine the morphological and compositional properties of a complex iron-based Fisher–Tropsch catalyst, as well as the properties and locations of the produced carbon species under working conditions. Chemical contour maps were constructed by processing STXM data files with an aXis2000 software package and revealed the compositional changes of catalysts during reactions, as shown in Fig. 7d–f: f. before treatment; e. after 2 h in H_2 at 350 °C; c. after 4 h in synthesis gas at 250 °C.[160]

5.2.3 Coherent X-ray diffraction imaging. The emergence of Coherent X-ray diffraction imaging (CXDI) has offered a highly advanced *in situ* and *operando* characterization approach to characterize structural properties of nanomaterials. So far, CXDI has demonstrated its ability to reveal 3D material morphologies, strains, and defects, as well as to probe surface adsorptions on catalysts at a spatial resolution of less than 10 nm.[162–168] In the CXDI process, an advanced X-ray source generates a spatially coherent X-ray beam, which then interacts with the sample and creates a far-field diffraction pattern. To cover the whole sample, the coherence volume of the beam should be larger than the sample size. Then, with an "oversampling" technique, a computational algorithm can retrieve the phase information from the diffraction. Traditionally, to obtain 3D diffraction patterns, the sample needs to be rotated to change the sample's angle to the beam. Afterwards, 3D images with material structural information are constructed from the obtained 3D diffraction data by a computer algorithm. So far, many optimization methods have been developed to enhance the performance of CXDI to meet the requirements for faster and simpler characterizations, including "chrono CDI" method to reduce the oversampling requirement,[168] and the "variable-wavelength" CDI method to construct 3D diffraction without rotating the sample.[166] This technology can bring unique opportunities for the studies of 2D materials for CO_2 ECR. For instance, strain engineering has been recently demonstrated to be an efficient strategy for enhancing the CO_2 ECR activity and selectivity, but the quantification of strain is still challenging.[169] By using CDI, Fernández *et al. in situ* monitored the strain change of single Pt nanoparticles upon exposure to O_2 and CO/O_2 mixtures.[170] An outstanding strain sensitivity of 10^{-4} was achieved to monitor the strain variation of the model catalyst with a 1-minute time resolution. They observed a tensile expansion of up to 0.09% in the nanoparticles when exposed to a O_2 environment and attributed this strain change to the formation of a platinum oxide that resulted in possible overheating of the sample and/or surface stress and lattice mismatch.[170] However, when a reducing environment was introduced by having an excessive amount of CO in the CO/O_2 gas mixture, compression started to occur, reducing the strain to less than 0.03%. Another *in situ* investigation on Pt nanoparticles conducted by Abuin and coworkers also examined the structural changes due to CO adsorption.[164] For the near surface region of the nanoparticle, a −0.01% strain was observed under Ar flow. However, in a mixed Ar/CO flow environment, the strain in the near surface region changed to +0.12%, suggesting that CO adsorption weakened the bonds among surface Pt atoms and thus generated an outward relaxation of these atoms. Consequently, new high index facets were created. Meanwhile, the bulk region exhibited a compressive strain of −0.15% under Ar flow and a decreased strain of −0.02% under AR/CO flow, implying CO-adsorption induced lattice expansion in the bulk region.[164] Fig. 8a illustrates the experiment setup and mechanism of CXDI characterization. Fig. 8b shows 3D CXDI imaging of Pt NP under (a) Ar flow and (b) mixed Ar/CO flow (c) probability density of the strain field in near surface region and (d) in the bulk.[164] In addition, they also found a good match between nanoparticle morphologies measured by *ex situ* AFM and *in situ* CXDI. As CO is an important product and intermediate in CO_2 ECR, such *in situ* studies using CXDI offered new aspects to be considered when studying and designing 2D materials for CO_2 ECR. Nevertheless, it must be pointed out that CXDI studies require advanced synchrotrons, which are mainly available at the 34-ID-C beamline at the APS, the EBS ID01 beamline at the ESRF, and a few others in Europe.

5.3 *In situ* and *operando* X-ray spectroscopy

5.3.1 *In situ* hard X-ray absorption spectroscopy. X-ray absorption spectroscopy (XAS) has been intensively used in catalytic reactions, including CO_2 ECR. In this characterization, X-ray beams generated by a light source interact with the sample and are partially absorbed. By measuring and plotting the absorption of X-rays as a function of photon energy, XAS can probe the dynamic changes in electronic structures of catalysts and thus be used for the studies of reaction mechanisms in CO_2 ECR processes. *In situ* and *operando* spectroscopy that probes the dynamic changes in a catalytic environment requires high intensity photons with a broad range of energies to construct highly resolved X-ray spectra. Usually, around 10^{10} photons per eV are needed, and this requirement can only be met by the use of synchrotrons to date.[172]

Hard X-rays with photon energies higher than 5 keV have strong penetration power. Consequently, hard X-ray absorption spectroscopy is highly desired *in situ* and *operando* studies that

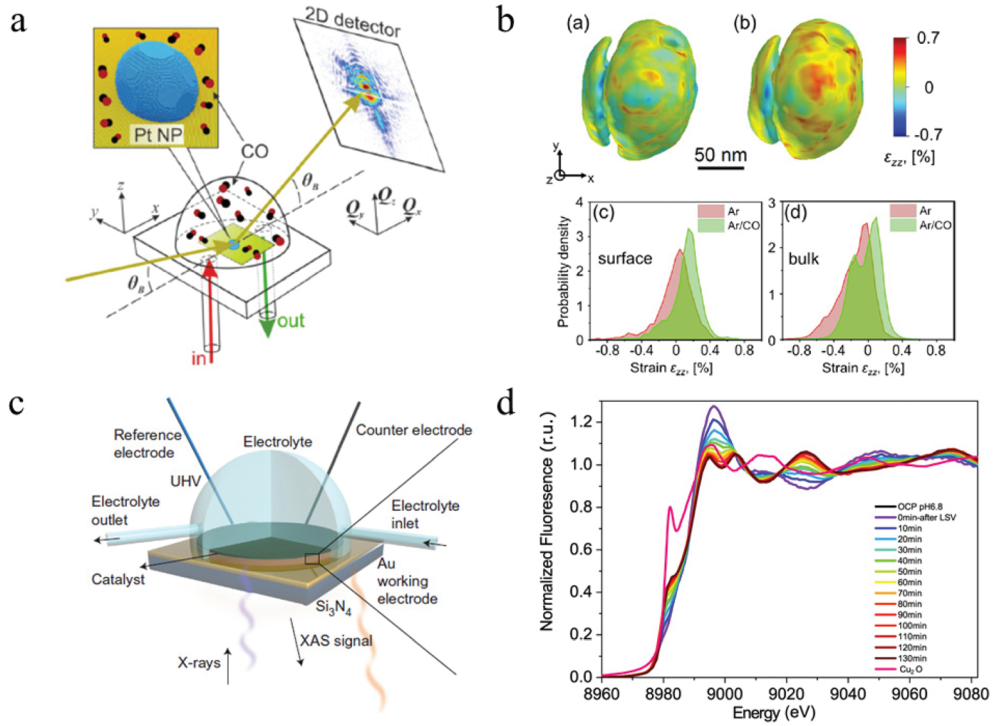

Fig. 8 (a) The schematic of CXDI imaging. (b) 3D CXDI imaging of Pt NP under different conditions and the strain field in near surface region and in the bulk. Copyright 2019, American Chemical Society; (c) *in situ* XAS electrochemical cell. Copyright 2017, Springer Nature; (d) time-resolved XAS spectrum. Copyright 2021, Springer Nature. All panels reproduced with permission.[153,164,171]

involve complex reaction environments with the presence of liquid, gas, and solid. In XAS, the absorption spectrum ranges immediately before and after the absorption edge is defined as the X-ray absorption near edge structure (XANES), which can characterize the density of states, thus revealing the valence states (at the absorption edge) and orbital hybridization due to coordination (pre-edge).[173] The extended X-ray absorption fine structure (EXAFS) covers the energy region above the absorption edge and can characterize the local atomistic structure, *i.e.*, the neighboring atoms to the bound atoms and the interatomic distances between them. For *in situ* and *operando* CO_2 ECR studies, specially designed electrochemical cells with X-ray windows are required to provide a reaction environment that can be characterized by both electrochemical workstations and XAS. Such windows are usually made from Si_3N_4 to ensure no blockage for X-ray to pass through. Fig. 8c shows a design of this cell.[171] *In situ* XAS has been utilized in the studies of 2D materials for CO_2 ECR as a powerful tool to probe the oxidation states and local coordination environment, thus determining the active sites during CO_2 electrochemical reduction reactions. For instance, a recent study on a bimetallic 2D conjugated metalorganic framework (2D c-MOF) demonstrated the synergistic effects between its CuN_4 ligand and ZnO_4 complex (ZnO_4) linkage with a high CO selectivity of 88%.[108] In this study, EXAFS spectrum showed an intensity decrease in Zn–O bond, suggesting interactions between ZnO_4 sites and reaction intermediates. With additional infrared absorption studies, the authors were able to conclude that ZnO_4 sites are catalytic reactive sites. Another investigation on 2D bismuth metal–organic framework employed *in situ* XAS to probe the stability of Bi^{3+} during CO_2 ECR. XANES analysis proved that the Bi^{3+} oxidation state stayed unchanged at a high potential of ~−0.9 V for 90 min, revealing a significantly enhanced Bi^{3+} stability in the prepared MOF structure than in other 2D materials.[104] Moreover, Wang and coworkers recently studied the highly selective CO_2 ECR reaction mechanism of 2D CuO nanosheet.[153] By using *in situ* XAS, they discovered that the CuO nanosheet gradually and directly converted into metallic Cu under a potential of −0.84 V (RHE) with no Cu_2O intermediates detected.[153] Fig. 8d shows the time-resolved information on the catalyst under a CO_2 ECR condition. EXAFS also showed that the coordination number of the produced Cu^0 is smaller than that in bulk fcc Cu^0, suggesting the existence of lattice defects associated with undercoordinated Cu atoms, which attributed to the enhanced efficiency and selectivity towards C_{2+} products. These in-depth mechanism studies demonstrated the abilities and advantages of *in situ* and *operando* XAS employed in CO_2 ECR studies using 2D materials.

5.3.2 *In situ* soft X-ray absorption spectroscopy. Soft X-rays absorption (sXAS) spectrum utilizes soft X-rays with energies below 5 keV and is a powerful tool to probe the structural properties of all the materials in a catalytic environment. For instance, the K-edge spectrum of the light elements such as carbon, nitrogen, and oxygen can be analyzed to study the

structural properties of 2D carbon-based catalysts and electrolytes.[103,174] Moreover, the L/M-edge spectrum of transition metals can be more sensitive to oxidation states than K-edge spectrum.[172] Additionally, soft XAS is very sensitive to the surface of solid materials and can reveal critical surface structure information, such as orbital hybridization, spin state, oxidation state, and adsorption species, *etc.* Heterogeneous catalysis mainly happens on the surface of solid catalysts, so the *operando* characterization of soft XAS is of vital importance to investigate the catalytic mechanism at atomic scales. Recently, many new discoveries and progresses made in CO_2 ECR investigations were benefited from *in situ* sXAS studies. Notably, *in situ* sXAS for the Cu L_3-edge demonstrated that the ratio and electronic state of copper species exhibited dynamic changes under different applied potentials in CO_2 ECR.[175] Time-resolved sXAS discovered that Cu^{2+} in $Cu_2(OH)_3Cl$ can be easily converted into Cu^+ species within 5 min of reaction, whereas the transition from Cu^+ to Cu^0 would take much longer time. This result suggested that the reduction of copper is hindered by oxychloride sol–gel, thus stabilizing Cu^+ species at more negative potentials.[175] Moreover, *in situ* sXAS has also been employed to probe the stabilization of other novel CO_2 catalysts, such as La_2CuO_4 perovskite nanocatalyst,[176] and demonstrated its great potential in the development of advanced CO_2 ECR catalysts. However, it must be pointed out that due to lower photon energies, the operation of soft XAS usually requires an ultra-high vacuum. Hence, the *in situ* and *operando* electrochemical cell needs to be well designed.

5.3.3 *In situ* X-ray photoelectron spectroscopy. X-ray photoelectron spectroscopy (XPS) is another powerful surface analysis tool that can probe the elemental compositions, chemical state, and electronic structures of the material surface. The operation of XPS is based on the photoelectric effect: the irradiation of X-rays can excite electrons and result in photoelectron emissions to the vacuum. By measuring the kinetic energy of emitted electrons, the bonding energy of these electrons can be quantified to identify the surface elements and their chemical states. However, due to the short mean free path of the emitted photoelectrons, XPS is mainly used to probe the surface properties within a few nanometers of depth, and the operation of XPS usually requires ultra-high vacuum conditions (UHV), which limits the used of XPS in *in situ* CO_2 ECR studies.[28] A few approaches have been proposed to counter this issue, including the use of membrane-sealed "environmental cells" and highly advanced near-ambient pressure XPS (NAP-XPS) that utilizes the differential pumping mechanism.[177–179] Similar to the microcells used in *in situ* TEM characterizations, the environmental cells can maintain atmospheric pressure within the cell while the whole cell is placed in a vacuum environment for XPS characterizations. The membranes, made of graphene oxide and other two-dimensional materials, are electron-transparent while strong enough to encapsulate all the reactants in the reaction environment.[179] In the differential pumping system, a set of pumping stages allows for an elevated pressure of a few millibars in the sample area, from where the pressure gradually decreased to a high vacuum level in the detector areal. Small apertures are used in such systems to maintain the pressure profile. Fig. 9a shows the mechanisms of these two approaches.[178]

In situ XPS has been employed in some fundamental studies to scrutinize CO_2 ECR mechanisms on different catalysts. For example, Favaro *et al.* used *in situ* ambient pressure X-ray photoelectron spectroscopy to investigate how subsurface oxide below Cu surface affects the CO_2 activation process.[180] *In situ* XPS examined the binding energy shifts of C 1s and O 1s photoelectron peaks on different surfaces. It was found that the presence of an optimal amount of subsurface oxide can form a mixed Cu^+ and Cu^0 structure that stabilized the bent CO_2, thus promoting the CO_2 activation.[180] Similarly, Kim and coworkers used *in situ* XPS to directly monitor the formation of dissociated CO* from chemisorbed CO_2 on Rh surfaces in a time-resolved manner.[181] Notably, this experiment was conducted under a 0.1 millibars environment. Fig. 9b shows the time-resolved monitoring of the formation of the dissociated CO adsorption on Rh surface.[181] Note that all the above examples used synchrotron radiation sources for the *in situ* ambient pressure XPS characterization, especially with the presence of liquid in the system. Synchrotron light sources can modulate the photon energy and thus characterize the samples in different depths, enabling both depth-resolved and time-resolved characterizations.[182]

5.4 Free electron laser (FEL) and "pump/probe" technique

Free Electron Lasers (FEL) can provide extremely coherent laser beams with ultrashort pulse duration (femtoseconds), ultrahigh brilliance, and widely turntable wavelengths ranging from microwave frequencies to hard X-rays.[184,185] They can generate much brighter electromagnetic radiation than other sources available nowadays.[186] With such unique advantages, FELs can be used for both imaging and spectroscopy, offering ultrafast time-resolved investigations of material properties and molecular dynamics with a temporal resolution in the scale of femtoseconds. In X-ray Free Electron Lasers (XFEL), a high energy relativistic electron beam is first generated by an electron source and then passes through a periodically alternating magnetic field, which is provided by the undulator/wiggler and forces the electrons to move along a sinusoidal path. The undulating motions of electrons then emit highly coherent radiations with wavelengths that can be modulated by the electron energy and/or the magnetic field strength. Fig. 9c illustrates the configuration of the FEL system.[183] There are only a few FEL facilities in the world nowadays, located in Asia, Europe, and the U.S.A. Notably, the European XFEL, located in Germany, has a high beam energy of 8.5–17.5 GeV and a short pulse duration of 3–150 fs. The photon energy is ranged from 240 eV to 25 000 eV, making it a powerful tool for probing various information mentioned above *in situ* catalytic investigations.

These unique advantages of FEL enable it to be used in the ultrafast pump/probe technique. In this technique, first, an

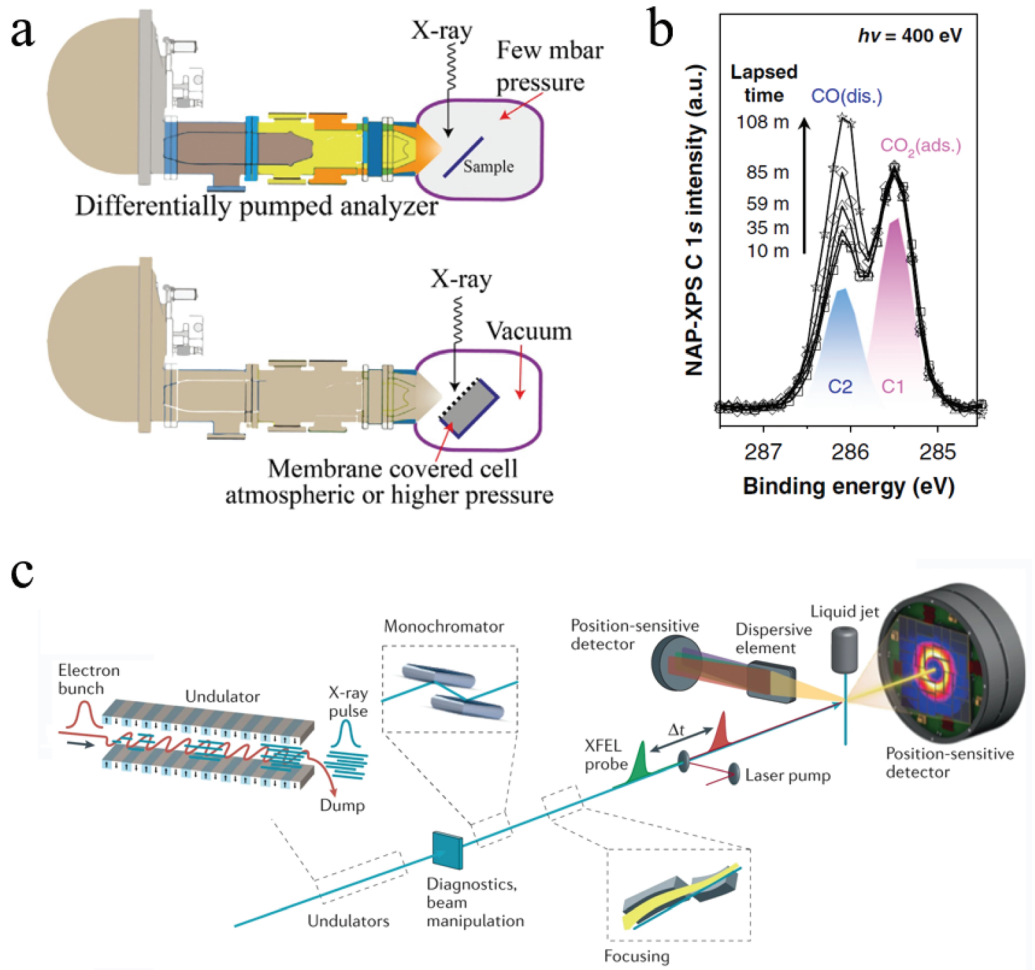

Fig. 9 (a) Two NAP-XPS systems: differential pumping system and environmental cell system. Copyright 2018, John Wiley and Sons. (b) Time resolved NAP-XPS showing the formation of dissociated CO absorption. Copyright 2020, Springer Nature; (c) configuration of the Free Electron Laser (FEL) system. Copyright 2021, Springer Nature. All panels reproduced with permission.[178,181,183]

ultrashort light pulse that lasts for less than 100 fs interacts with the material and initiates photochemical reactions, thus exciting the system to a non-equilibrium state. This step is called the "pump" step. Then the non-equilibrium state is probed by a following ultrashort light pulse that monitors the changes that occurred due to the excitation. The temporal intervals of these two pulses can be modulated to investigate the time-dependent dynamics of the reactions. Besides using coherent X ray as pump and probe, the ultrafast electron diffraction (UED) use the laser pump and electron beam probe to study the molecular structural dynamics.[187] Consequently, the field of "femtochemistry" was constructed to investigate the fundamental reaction mechanisms in chemical reactions.[188] The pump and probe technique have been adopted in CO_2RR studies to mainly investigate the carrier dynamics of photocatalysts, as such systems can be easily excited by pump pulses.[189,190] However, many other reactants and catalysts in other catalytic systems cannot be excited by light pulses. Fortunately, hopes for probing electrocatalytic reactions have been brought by some pioneering studies. Ultrafast XAS, which can be realized by the pump/probe spectroscopy, has been utilized in the *in situ* monitoring of the sub-femtosecond motions of valence electrons. The monitoring of such motions can help reveal the fundamental reaction mechanism of CO_2 ECR using 2D materials.

5.5 Other *in situ* and *operando* spectrometry

5.5.1 *In situ* and *operando* mass spectrometry. Mass spectrometry (MS) is an efficient, sensitive, and accurate method to probe the catalytic intermediates and products during CO_2 ECR, offering deep understandings of the reaction dynamics and mechanisms. Unlike liquid chromatography and gas chromatography, which require minutes of time for analytes to flow through columns, MS measures the mass-to-charge ratios of ionized samples with a temporal resolution on the scale of a second.[191] Hence, online electrochemical MS techniques, especially Differential Electrochemical Mass Spectrometry (DEMS), have been adopted in *in situ* studies to directly probe reaction products and, therefore, the local reaction environment on the electrode–electrolyte interfaces in CO_2 ECR.[192]

DEMS is constructed with a three-electrode electrochemistry cell, a porous PTFE membrane that lets the gaseous products flow through, and a vacuum system that connects to the MS. DEMS can help probe the potential-dependent activity and selectivity of catalysts in a time-resolved manner.[193] Remarkably, online MS can be combined with other *operando* characterization tools, such as TEM, to construct the structure–activity relationships of various catalysts.[124,194] Using this technique, Clark *et al.* demonstrated the direct observation of ten different reaction species in CO_2 ECR with Ag and Cu catalysts.[192] Through the direct sample collection at the electrode–electrolyte interface, *in situ* DEMS probed larger amounts of aldehydes than that characterized by *ex situ* methods in bulk samples.[192] This demonstrates better products collection efficiency by using *in situ* methods rather than traditional *ex situ* methods. This should be considered in the experimental design and when quantifying the efficiency and selectivity of the catalyst. Additionally, there were 2–4 times more aldehydes than the corresponding alcohols.[192] Such results suggested that these aldehydes are reduced to corresponding alcohols prior to entering into the bulk electrolytes in CO_2 ECR. The potential-dependent product distribution was also characterized. Even though *in situ* MS has been utilized in many studies, future optimizations are still required to further improve the temporal and spatial resolutions.[195]

5.5.2 *In situ* and *operando* infrared spectroscopy. *Operando* Infrared (IR) spectroscopy can monitor and analyze the reaction intermediates and products in real-time with relatively high temporal resolutions, greatly benefiting the investigations on CO_2 ECR reaction mechanisms and catalytic sites.[196] The operation of IR is based on the specific absorptions of mid-infrared beams by molecules where the characteristic vibrational modes of molecules match the beam energies. Four operation modes are available for *in situ* or *operando* IR characterizations in catalytic reactions, including external-reflectance (*i.e.*, infrared reflection absorption spectroscopy, IRAS), attenuated total reflection (ATR), diffuse reflectance FT-IR spectroscopy (DRIFTS), and transmission (TIR).[197] In electrocatalytic systems that involve liquid electrolytes, the high infrared absorption of water and ionic liquids can interfere with such IR characterizations. Therefore, it is critical to shorten the path length of IR beams in *in situ* IR measurements. This requirement has made ATR and IRAS particularly suitable for *in situ* IR characterizations for electrochemical reactions. In IRAS, the tip of the working electrode, on which the electrochemical reactions take place, is placed facing an infrared-transparent window that only 1–10 μm of electrolyte layers present between the electrode and window. The IR beams then transmit through the window for measurements. Hence, the interference caused by electrolytes can be minimized.[196] ATR-IR adopts the Kretschmann configuration for attenuated total reflection. The working electrode is deposited as a thin film on an infrared-transparent prism, which allows the IR reach total internal reflection when the IR beam is placed at an angle of incidence larger than the critical angle. Thus, the IR beams do not pass through the liquid electrolyte and instead penetrate the liquid only by the depth of 1–2 μm through the evanescent wave to interact with adsorbed molecules on the surface of electrocatalysts.[198]

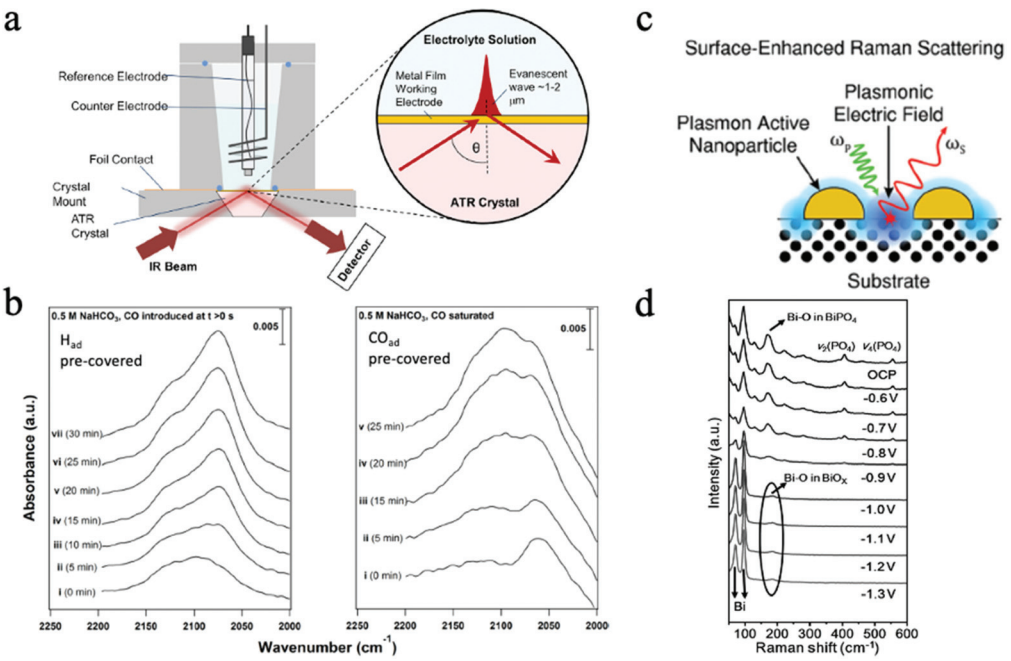

Fig. 10 (a) Mechanism of *in situ* ATR. Copyright 2017, crown; (b) time-resolved SEIRA spectra of H_{ad} accumulation on CO-adsorbed Cu surface. Copyright 2016, American Chemical Society (c) mechanism of SERS. Copyright 2021, Royal Society of Chemistry; (d) *operando* Raman spectra under different applied potential. All panels reproduced with permission.[198–201] Copyright 2021, 2021 Wiley and Sons.

Fig. 10a illustrates the mechanism of this advanced technique. By combing ATR and the Surface Enhanced Infrared Absorption Spectroscopy (SEIRAS), ATR-SEIRAS has demonstrated enhanced time resolution and sensitivity for *operando* studies, less interference from the bulk electrolyte, and the reduced IR attenuation and transport limitations.[196] The high IR absorption cross-section of C–O bonds makes IR very suitable for CO_2 ECR studies that produce formate, CO, as well as other common intermediates and products in CO_2RR.[198] SEIRAS has been widely utilized in CO_2 ECR studies for the investigations of fundamental reaction mechanisms and reaction species. For instance, SEIRAS demonstrated that the adsorbed hydrogen could partially displace adsorbed carbon monoxide on the Cu surface during CO_2RR, while the displacement can't occur in the reversed direction. Hence, it was proposed that hydrogen has a higher absorption strength than that of CO.[199]

Fig. 10b shows the time-resolved SEIRA spectra of hydrogen and CO on H_{ad} pre-covered and CO pre-covered Cu surfaces, proving that hydrogen can displace adsorbed carbon monoxide.[199] Additionally, SEIRS also revealed that the surface C-bound and O-bound reaction intermediates can affect the overall CO_2RR reaction selectivity. Regardless of the powerful characterization ability, one drawback of *in situ* and *operando* IR in catalytic reactions is the limited access to low wavenumbers, which can help obtain information on the structural properties of surface oxides and hydroxides.[196] Moreover, the focused IR beam area is on the micron scale, which is relatively large for precisely probing nanomaterials. Hence, the measured peak only shows the averaged data within the whole beam area.

5.5.3 *In situ* and *operando* electrochemical Raman spectroscopy. Advanced *in situ* electrochemical Raman spectroscopy (RS), including surface-enhanced Raman scattering (SERS), shell-isolated nanoparticle-enhanced Raman spectroscopy (SHINERS), and tip-enhanced Raman spectroscopy (TERS), is a powerful and nondestructive tool to monitor the catalyst states and probe the reaction intermediates and products during catalytic reactions.[28] The operation of Raman spectroscopy is based on the Raman scattering, *i.e.*, the inelastic scattering of incoming photons due to the interactions between incoming monochromatic light beams and chemical bonds, resulting in wavelength shifts. Raman spectroscopy (RS) is complementary to IR. However, unlike the absorption-based IR, the scattering-based RS better suits the characterizations of an aqueous environment, as water doesn't induce strong Raman scattering.[200] In *in situ* RS, the beam is introduced by a confocal system and interacts with the catalyst surface after passing through an observation window, through which the scattered signal is also collected using a reflective mirror.

Fig. 10c illustrates the schematic of this operation. As an enhanced technique, SERS operates based on the SERS enhancement effects, which are induced by the amplified local electric field as a result of the resonant excitations of surface plasmons and the non-resonant lightning rod effects due to the concentrated field at enhancement sources, *i.e.*, surface features that maximize electromagnetic enhancement.[198] A significant enhancement in the Raman signal can be achieved in this way, making this technique highly desired in catalytic reactions to monitor the surface absorbates and reaction species.[200] Nevertheless, the dominant enhancement sources can also interfere with the characteristic signals from samples. Consequently, SHINERS was developed to isolate the enhancement sources (such as sharp tip/surfaces) to minimize the interference, making SERS applicable to all kinds of surfaces and morphologies.[202] On the other hand, by combing SERS and scanning probe microscopy tips, tip-enhanced Raman spectroscopy (TERS) was introduced to provide highly sensitive and spatial-resolved characterizations by involving a scanning probe microscopy tip. With a spatial resolution as high as 1–10 nm, TERS is extremely helpful in *in situ* characterizations of nanocatalysts.[203,204] *In situ* Raman characterizations have been demonstrated with different 2D materials for CO_2 ECR and provided information on the reaction mechanisms and reactive sites. For example, in a recent study, bismuth phosphate ($BiPO_4$)-derived 2D Nanosheets were examined by *operando* Raman spectroscopy during CO_2 ECR at different potentials. As shown in Fig. 10d, the disappeared Raman peaks associated with the PO_4 group and the shifts of peaks assigned to Bi–O bond suggested the formation of Bi and BiO_x during CO_2 ECR.[201] The abundance of Bi–O on the surface was attributed to the enhanced CO_2 ECR performance. Many reaction intermediates, such as *CO and *HCOO, have been identified in *in situ* studies as key intermediates in CO_2 ECR.[201] Even though TERS is a highly advanced *in situ* characterization technique, many limitations, such as the short tip lifetime and the inability to characterize single-molecule level features, still need to be overcome in the future.[203] Similar to IR, Raman spectroscopy is also limited by the large beam area with average data when characterizing nanomaterials, which make lack the heterogeneity information from samples.

6 Challenges and outlook

In recent years, 2D materials have been intensively investigated and utilized in CO_2 electrochemical reductions to value-added products. With the emergence of many innovative 2D catalysts, exceptional progress has been achieved *via* various approaches to enhance the activity, selectivity, and overall performance of such 2D catalysts, providing promising paradigms for the next generation CO_2 conversion systems. Nevertheless, the development of 2D catalysts for CO_2 ECR still faces many challenges, bringing promising opportunities in this field of study. Most of the current studies are only focused on the catalyst material aspects, such as the types of materials, morphologies, defects, and compositions. However, catalytic systems are often very complex and include numerous components that need to be integrated into the studies of 2D catalysts. Many parameters, including the reactor design, electrolytes, and local reaction

environment, can all determine the overall CO_2 ECR performance.

In CO_2 ECR, the local reaction environment can be constructed by both solid/liquid and solid/gas/liquid interfaces. With the adsorption, reaction, and desorption all taking place at these interfaces, these reactions are all governed by the synergistic effects of all the components in the local environment. It has been reported that the interactions between solutions and reactants can critically affect CO_2 performance. For instance, the types and sizes of both anions and cations in electrolytes have demonstrated governing effects on the selectivity of CO_2 ECR *via* affecting the adsorptions of reaction intermediates, altering the charge distributions on catalysts surface, and shifting the reaction free-energy landscape of Cu catalysts.[205–207] Moreover, the electrical fields created in the Helmholtz layer and the use of ionic liquids have demonstrated various effects.[208,209] Organic surfactants like cetyltrimethylammonium bromide have also enhanced CO_2 ECR performance by inhibiting the competing HER at the catalyst surface.[210] The interactions between liquid electrolytes and solid catalysts and the generated liquid–solid interfaces can all determine the CO_2 ECR performance. With their unique 2D morphologies and substantial dopant and vacancy exposures, 2D nanocatalysts might induce distinctive reaction behaviors in such a highly localized reaction environment. Such investigations on the local reaction environment are required to enhance the performance of 2D CO_2 catalysts further.

Researchers might also investigate additional novel enhancing strategies, such as catalyst modifiers and strain engineering, in the study of 2D materials. Recently, polymers have shown exceptional optimizing capabilities by modulating the heterogeneous catalytic surfaces and stabilizing metal nanocatalysts.[211–213] Hydrophilic polymeric modifiers can enhance the selectivity for formic acid, while cationic hydrophobic modifiers can promote the formation of CO on Cu catalysts.[212] Moreover, polymeric N-heterocyclic carbenes (NHC), such as polydentate and monodentate, have exhibited stabilizing effects on Au and Pd nanocatalysts due to the formation of metal–carbene bonds that inhibit the nanoclustering of nanoparticles.[211] Such findings especially pertain to the use of 2D catalysts. The mechanisms and approaches proposed in novel optimization paradigms may also be applied to 2D nanocatalysts to achieve organic modifications at the atomic scale. Lattice strains have demonstrated the potential to alter the band structures of 2D materials and break the linear scaling relationship for CO_2 ECR, thus enhancing the selectivity and activity.[214,215] However, it is still challenging to scrutinize the underlying mechanisms due to the difficulties of decoupling strain from other electronic effects in 2D materials with mismatched lattice.[169] More simulation and experimental approaches need to be combined to investigate such optimization behaviors. Additionally, applying strain on 2D catalysts with desired magnitude and distribution remains difficult to realize.

With the introduction of gas diffusion layers and polymer ion-exchange membranes in membrane electrode assembly (MEA) electrolyzers, gas-phase electrolyzers have enhanced the current density and stability of CO_2 ECR.[105] Remarkably, some novel all-solid-state reactors that utilize polymer electrolytes can significantly facilitate the separation of liquid products in continuous productions.[114] However, to date, most investigations on 2D catalysts have been conducted in liquid phase electrolyzers. The opportunities brought by such advanced reactors need to be seized in the study of 2D materials for CO_2 ECR. It must be pointed out that, in these solid-state reactors, the interactions between solid catalysts and solid electrolytes, the adsorption, desorption, and the mass transport of reaction species, as well as the local reaction environment are all different at the solid–solid interfaces from those at traditional liquid–solid interfaces. The behaviors and performance of 2D nanocatalysts in these advanced reaction environments and reactors need to be characterized and optimized to achieve superior CO_2 ECR efficiency and selectivity in future industrial-scale CO_2 ECR systems.

Due to the complexity of the catalytic reactions, many scientific problems cross orders of magnitude in times and length scales. Thus, we urge to use *in situ* and *operando* multimodal characterizations to get comprehensive, insightful information across different characterization platforms. Advanced *in situ* and *operando* multimodal characterizations of 2D nanocatalysts can help achieve fundamental understandings of CO_2 ECR mechanisms, especially when coupled with modern DFT calculations. Even though such characterizations often require advanced facilities such as synchrotron X-ray sources, electron microscopy, and free electron laser, the information corrected can reveal the underlying reaction active sites, pathways, intermediates, local environment, and morphological changes of 2D catalysts. Therefore, it is essential to actively employ *operando* multimodal characterizations in future studies to better design 2D nanocatalysts and beyond. More importantly, such *in situ* and *operando* characterizations conducted in flow cells and MEA electrolyzers remain extremely challenging. To develop 2D nanocatalysts used in industrial scale electrolyzers, specially designed apparatuses are highly demanded by *in situ* and *operando* studies.

Finally, to realize the utilization of 2D materials in real-life, industrial-scale CO_2 conversion systems, the mass production of 2D materials with high efficiencies, high selectivity and high stability must be achieved in the coming future. Yet, the production of 2D nanomaterials is still very challenging due to the aggregation and restacking caused by electrostatic and van der Waals interactions. Moreover, the productivity is still too low to achieve cost-effective productions and utilizations of 2D materials for CO_2 conversion. On the other hand, the feasibility of mass production should be kept in mind when designing next-generation 2D nanocatalysts.

Conflicts of interest

The authors do not have conflict of interests to declare.

Acknowledgements

Yimin A. Wu thanks funding support from Natural Sciences and Engineering Research Council of Canada (NSERC) (RGPIN-2020-05903, GECR-2020-00476), and National Research Council of Canada Materials for Clean Fuels Challenge Program (CH-MCF-123). Cheng Du acknowledges the support from CUTRIC (Canadian Urban Transit Research & Innovation Consortium) through a MITACS accelerate postdoc program.

References

1 C. D. Thomas, A. Cameron, R. E. Green, M. Bakkenes, L. J. Beaumont, Y. C. Collingham, B. F. Erasmus, M. F. De Siqueira, A. Grainger, L. Hannah, L. Hughes, B. Huntley, A. S. Van Jaarsveld, G. F. Midgley, L. Miles, M. A. Ortega-Huerta, A. T. Peterson, O. L. Phillips and S. E. Williams, *Nature*, 2004, **427**, 145–148.
2 P. M. Cox, R. A. Betts, C. D. Jones, S. A. Spall and I. J. Totterdell, *Nature*, 2000, **408**, 184–187.
3 Z. Y. Sun, T. Ma, H. C. Tao, Q. Fan and B. X. Han, *Chem*, 2017, **3**, 560–587.
4 S. Garg, M. Li, A. Z. Weber, L. Ge, L. Li, V. Rudolph, G. Wang and T. E. Rufford, *J. Mater. Chem. A*, 2020, **8**, 1511–1544.
5 S. Nitopi, E. Bertheussen, S. B. Scott, X. Liu, A. K. Engstfeld, S. Horch, B. Seger, I. E. L. Stephens, K. Chan, C. Hahn, J. K. Norskov, T. F. Jaramillo and I. Chorkendorff, *Chem. Rev.*, 2019, **119**, 7610–7672.
6 L. Fan, C. Xia, F. Yang, J. Wang, H. Wang and Y. Lu, *Sci. Adv.*, 2020, **6**, eaay3111.
7 R. Kortlever, J. Shen, K. J. Schouten, F. Calle-Vallejo and M. T. Koper, *J. Phys. Chem. Lett.*, 2015, **6**, 4073–4082.
8 D. F. Gao, R. M. Aran-Ais, H. S. Jeon and B. Roldán Cuenya, *Nat. Catal.*, 2019, **2**, 198–210.
9 C. Du, X. Wang, W. Chen, S. Feng, J. Wen and Y. A. Wu, *Mater. Today Adv.*, 2020, **6**, 24.
10 F. P. Pan and Y. Yang, *Energy Environ. Sci.*, 2020, **13**, 2275–2309.
11 Y. Hori, K. Kikuchi and S. Suzuki, *Chem. Lett.*, 1985, 1695–1698, DOI: 10.1246/cl.1985.1695.
12 R. Kortlever, I. Peters, C. Balemans, R. Kas, Y. Kwon, G. Mul and M. T. Koper, *Chem. Commun.*, 2016, **52**, 10229–10232.
13 J. L. Qiao, Y. Y. Liu, F. Hong and J. J. Zhang, *Chem. Soc. Rev.*, 2014, **43**, 631–675.
14 J. Hawecker, J.-M. Lehn and R. Ziessel, *J. Chem. Soc., Chem. Commun.*, 1984, 328–330, DOI: 10.1039/c39840000328.
15 D. Sun, X. Xu, Y. Qin, S. P. Jiang and Z. Shao, *ChemSusChem*, 2020, **13**, 39–58.
16 A. Salehi-Khojin, H. R. M. Jhong, B. A. Rosen, W. Zhu, S. C. Ma, P. J. A. Kenis and R. I. Masel, *J. Phys. Chem. C*, 2013, **117**, 1627–1632.
17 R. Reske, H. Mistry, F. Behafarid, B. Roldán Cuenya and P. Strasser, *J. Am. Chem. Soc.*, 2014, **136**, 6978–6986.
18 H. Mistry, R. Reske, Z. Zeng, Z. J. Zhao, J. Greeley, P. Strasser and B. R. Cuenya, *J. Am. Chem. Soc.*, 2014, **136**, 16473–16476.
19 H. Mistry, R. Reske, P. Strasser and B. Roldán Cuenya, *Catal. Today*, 2017, **288**, 30–36.
20 H. S. Jeon, I. Sinev, F. Scholten, N. J. Divins, I. Zegkinoglou, L. Pielsticker and B. R. Cuenya, *J. Am. Chem. Soc.*, 2018, **140**, 9383–9386.
21 Y. Sun, S. Gao, F. Lei and Y. Xie, *Chem. Soc. Rev.*, 2015, **44**, 623–636.
22 H. Tao, Y. Gao, N. Talreja, F. Guo, J. Texter, C. Yan and Z. Sun, *J. Mater. Chem. A*, 2017, **5**, 7257–7284.
23 W. Bi, X. Li, R. You, M. Chen, R. Yuan, W. Huang, X. Wu, W. Chu, C. Wu and Y. Xie, *Adv. Mater.*, 2018, **30**, e1706617.
24 Z. Lin, B. R. Carvalho, E. Kahn, R. Lv, R. Rao, H. Terrones, M. A. Pimenta and M. Terrones, *2D Mater.*, 2016, **3**, 022002.
25 H. Chen, A. D. Handoko, J. Xiao, X. Feng, Y. Fan, T. Wang, D. Legut, Z. W. Seh and Q. Zhang, *ACS Appl. Mater. Interfaces*, 2019, **11**, 36571–36579.
26 F. P. García De Arquer, O. S. Bushuyev, P. De Luna, C.-T. Dinh, A. Seifitokaldani, M. I. Saidaminov, C.-S. Tan, L. N. Quan, A. Proppe, M. G. Kibria, S. O. Kelley, D. Sinton and E. H. Sargent, *Adv. Mater.*, 2018, **30**, 1802858.
27 H. Cheng, S. Liu, J. Zhang, T. Zhou, N. Zhang, X. S. Zheng, W. Chu, Z. Hu, C. Wu and Y. Xie, *Nano Lett.*, 2020, **20**, 6097–6103.
28 A. D. Handoko, F. X. Wei, Jenndy, B. S. Yeo and Z. W. Seh, *Nat. Catal.*, 2018, **1**, 922–934.
29 K. F. Kalz, R. Kraehnert, M. Dvoyashkin, R. Dittmeyer, R. Glaser, U. Krewer, K. Reuter and J. D. Grunwaldt, *ChemCatChem*, 2017, **9**, 17–29.
30 R. Zhou, X. Fan, X. Ke, J. Xu, X. Zhao, L. Jia, B. Pan, N. Han, L. Li, X. Liu, J. Luo, H. Lin and Y. Li, *Nano Lett.*, 2021, **21**, 4092–4098.
31 Y. Lan, G. Niu, F. Wang, D. Cui and Z. Hu, *ACS Appl. Mater. Interfaces*, 2020, **12**, 36128–36136.
32 W. Huang, D. Zhou, H. Yang, X. Liu and J. Luo, *ACS Appl. Energy Mater.*, 2021, **4**, 7492–7496.
33 Q. Zhao, C. Zhang, R. Hu, Z. Du, J. Gu, Y. Cui, X. Chen, W. Xu, Z. Cheng, S. Li, B. Li, Y. Liu, W. Chen, C. Liu, J. Shang, L. Song and S. Yang, *ACS Nano*, 2021, **15**, 4927–4936.
34 C. Cao, D. D. Ma, J. Jia, Q. Xu, X. T. Wu and Q. L. Zhu, *Adv. Mater.*, 2021, **33**, 2008631.
35 M. Cokoja, C. Bruckmeier, B. Rieger, W. A. Herrmann and F. E. Kuhn, *Angew. Chem., Int. Ed.*, 2011, **50**, 8510–8537.
36 W. J. Zhang, Y. Hu, L. B. Ma, G. Y. Zhu, P. Y. Zhao, X. L. Xue, R. P. Chen, S. Y. Yang, J. Ma, J. Liu and Z. Jin, *Nano Energy*, 2018, **53**, 808–816.
37 H. Zhang, Y. Ma, F. J. Quan, J. J. Huang, F. L. Jia and L. Z. Zhang, *Electrochem. Commun.*, 2014, **46**, 63–66.

38 P. Su, W. Xu, Y. Qiu, T. Zhang, X. Li and H. Zhang, *ChemSusChem*, 2018, **11**, 848–853.
39 L. C. Yi, J. X. Chen, P. Shao, J. H. Huang, X. X. Peng, J. W. Li, G. X. Wang, C. Zhang and Z. H. Wen, *Angew. Chem., Int. Ed.*, 2020, **59**, 20112–20119.
40 H. Yang, N. Han, J. Deng, J. Wu, Y. Wang, Y. Hu, P. Ding, Y. Li, Y. Li and J. Lu, *Adv. Energy Mater.*, 2018, **8**, 1801536.
41 C. J. Peng, G. Zeng, D. D. Ma, C. Cao, S. Zhou, X. T. Wu and Q. L. Zhu, *ACS Appl. Mater. Interfaces*, 2021, **13**, 20589–20597.
42 C.-Y. Lee, Y. Zhao, C. Wang, D. R. G. Mitchell and G. G. Wallace, *Sustainable Energy Fuels*, 2017, **1**, 1023–1027.
43 T. T. Zhang, X. F. Li, Y. L. Qiu, P. P. Su, W. B. Xu, H. X. Zhong and H. M. Zhang, *J. Catal.*, 2018, **357**, 154–162.
44 J. Pan, Y. M. Sun, P. L. Deng, F. Yang, S. H. Chen, Q. Zhou, H. S. Park, H. F. Liu and B. Y. Xia, *Appl. Catal., B*, 2019, **255**, 117736.
45 L. Dai, Q. Qin, P. Wang, X. Zhao, C. Hu, P. Liu, R. Qin, M. Chen, D. Ou, C. Xu, S. Mo, B. Wu, G. Fu, P. Zhang and N. Zheng, *Sci. Adv.*, 2017, **3**, e1701069.
46 W. Zhang, Q. Qin, L. Dai, R. Qin, X. Zhao, X. Chen, D. Ou, J. Chen, T. T. Chuong, B. Wu and N. Zheng, *Angew. Chem., Int. Ed.*, 2018, **57**, 9475–9479.
47 W. Deng, L. Zhang, L. Li, S. Chen, C. Hu, Z. J. Zhao, T. Wang and J. Gong, *J. Am. Chem. Soc.*, 2019, **141**, 2911–2915.
48 M. F. Baruch, J. E. Pander, J. L. White and A. B. Bocarsly, *ACS Catal.*, 2015, **5**, 3148–3156.
49 A. Dutta, A. Kuzume, V. Kaliginedi, M. Rahaman, I. Sinev, M. Ahmadi, B. Roldán Cuenya, S. Vesztergom and P. Broekmann, *Nano Energy*, 2018, **53**, 828–840.
50 S. Gao, Y. Lin, X. Jiao, Y. Sun, Q. Luo, W. Zhang, D. Li, J. Yang and Y. Xie, *Nature*, 2016, **529**, 68–71.
51 J. Jia, C. Qian, Y. Dong, Y. F. Li, H. Wang, M. Ghoussoub, K. T. Butler, A. Walsh and G. A. Ozin, *Chem. Soc. Rev.*, 2017, **46**, 4631–4644.
52 S. Gao, X. Jiao, Z. Sun, W. Zhang, Y. Sun, C. Wang, Q. Hu, X. Zu, F. Yang, S. Yang, L. Liang, J. Wu and Y. Xie, *Angew. Chem., Int. Ed.*, 2016, **55**, 698–702.
53 F. Li, L. Chen, G. P. Knowles, D. R. MacFarlane and J. Zhang, *Angew. Chem., Int. Ed.*, 2017, **56**, 505–509.
54 S. Gao, Z. Sun, W. Liu, X. Jiao, X. Zu, Q. Hu, Y. Sun, T. Yao, W. Zhang, S. Wei and Y. Xie, *Nat. Commun.*, 2017, **8**, 14503.
55 Z. Geng, X. Kong, W. Chen, H. Su, Y. Liu, F. Cai, G. Wang and J. Zeng, *Angew. Chem., Int. Ed.*, 2018, **57**, 6054–6059.
56 N. Sakai, Y. Ebina, K. Takada and T. Sasaki, *J. Am. Chem. Soc.*, 2004, **126**, 5851–5858.
57 X. Y. Chen, Y. Zhou, Q. Liu, Z. D. Li, J. G. Liu and Z. G. Zou, *ACS Appl. Mater. Interfaces*, 2012, **4**, 3372–3377.
58 Y. Zhou, Z. P. Tian, Z. Y. Zhao, Q. Liu, J. H. Kou, X. Y. Chen, J. Gao, S. C. Yan and Z. G. Zou, *ACS Appl. Mater. Interfaces*, 2011, **3**, 3594–3601.
59 Q. Liu, D. Wu, Y. Zhou, H. Su, R. Wang, C. Zhang, S. Yan, M. Xiao and Z. Zou, *ACS Appl. Mater. Interfaces*, 2014, **6**, 2356–2361.
60 S. Y. Zhu, S. J. Liang, J. H. Bi, M. H. Liu, L. M. Zhou, L. Wu and X. X. Wang, *Green Chem.*, 2016, **18**, 1355–1363.
61 S. Gao, B. Gu, X. Jiao, Y. Sun, X. Zu, F. Yang, W. Zhu, C. Wang, Z. Feng, B. Ye and Y. Xie, *J. Am. Chem. Soc.*, 2017, **139**, 3438–3445.
62 M. Asadi, B. Kumar, A. Behranginia, B. A. Rosen, A. Baskin, N. Repnin, D. Pisasale, P. Phillips, W. Zhu, R. Haasch, R. F. Klie, P. Kral, J. Abiade and A. Salehi-Khojin, *Nat. Commun.*, 2014, **5**, 4470.
63 M. Asadi, K. Kim, C. Liu, A. V. Addepalli, P. Abbasi, P. Yasaei, P. Phillips, A. Behranginia, J. M. Cerrato, R. Haasch, P. Zapol, B. Kumar, R. F. Klie, J. Abiade, L. A. Curtiss and A. Salehi-Khojin, *Science*, 2016, **353**, 467–470.
64 P. Abbasi, M. Asadi, C. Liu, S. Sharifi-Asl, B. Sayahpour, A. Behranginia, P. Zapol, R. Shahbazian-Yassar, L. A. Curtiss and A. Salehi-Khojin, *ACS Nano*, 2017, **11**, 453–460.
65 J. Xu, X. Li, W. Liu, Y. Sun, Z. Ju, T. Yao, C. Wang, H. Ju, J. Zhu, S. Wei and Y. Xie, *Angew. Chem., Int. Ed.*, 2017, **56**, 9121–9125.
66 X. Hong, K. R. Chan, C. Tsai and J. K. Nørskov, *ACS Catal.*, 2016, **6**, 4428–4437.
67 X. Jiao, Z. Chen, X. Li, Y. Sun, S. Gao, W. Yan, C. Wang, Q. Zhang, Y. Lin, Y. Luo and Y. Xie, *J. Am. Chem. Soc.*, 2017, **139**, 7586–7594.
68 X. D. Li, Y. F. Sun, J. Q. Xu, Y. J. Shao, J. Wu, X. L. Xu, Y. Pan, H. X. Ju, J. F. Zhu and Y. Xie, *Nat. Energy*, 2019, **4**, 690–699.
69 X. Jiao, X. Li, X. Jin, Y. Sun, J. Xu, L. Liang, H. Ju, J. Zhu, Y. Pan, W. Yan, Y. Lin and Y. Xie, *J. Am. Chem. Soc.*, 2017, **139**, 18044–18051.
70 L. D. Ramírez-Valencia, E. Bailón-García, F. Carrasco-Marín and A. F. Pérez-Cadenas, *Catalysts*, 2021, **11**, 351.
71 H. Jin, C. Guo, X. Liu, J. Liu, A. Vasileff, Y. Jiao, Y. Zheng and S. Z. Qiao, *Chem. Rev.*, 2018, **118**, 6337–6408.
72 G. L. Chai and Z. X. Guo, *Chem. Sci.*, 2016, **7**, 1268–1275.
73 H. Wang and J. M. Lee, *J. Mater. Chem. A*, 2020, **8**, 10604–10624.
74 Y. Gogotsi and B. Anasori, *ACS Nano*, 2019, **13**, 8491–8494.
75 J. L. Hart, K. Hantanasirisakul, A. C. Lang, B. Anasori, D. Pinto, Y. Pivak, J. T. Van Omme, S. J. May, Y. Gogotsi and M. L. Taheri, *Nat. Commun.*, 2019, **10**, 522.
76 N. Li, X. Chen, W. J. Ong, D. R. MacFarlane, X. Zhao, A. K. Cheetham and C. Sun, *ACS Nano*, 2017, **11**, 10825–10833.
77 A. D. Handoko, K. H. Khoo, T. L. Tan, H. M. Jin and Z. W. Seh, *J. Mater. Chem. A*, 2018, **6**, 21885–21890.
78 Y. Xiao and W. Zhang, *Nanoscale*, 2020, **12**, 7660–7673.
79 H. Furukawa, K. E. Cordova, M. O'Keeffe and O. M. Yaghi, *Science*, 2013, **341**, 1230444.
80 X. X. Tang, L. Zhao, W. W. Sun and Y. Wang, *J. Power Sources*, 2020, **477**, 228919.

81 M. K. Lee, M. Shokouhimehr, S. Y. Kim and H. W. Jang, *Adv. Energy Mater.*, 2021, 2003990, DOI: 10.1002/aenm.202003990.
82 Q. Y. Cui, G. Q. Qin, W. H. Wang, K. R. Geethalakshmi, A. J. Du and Q. Sun, *Appl. Surf. Sci.*, 2020, **500**, 143993.
83 H. Zhong, M. Ghorbani-Asl, K. H. Ly, J. Zhang, J. Ge, M. Wang, Z. Liao, D. Makarov, E. Zschech, E. Brunner, I. M. Weidinger, J. Zhang, A. V. Krasheninnikov, S. Kaskel, R. Dong and X. Feng, *Nat. Commun.*, 2020, **11**, 1409.
84 S. Lin, C. S. Diercks, Y. B. Zhang, N. Kornienko, E. M. Nichols, Y. Zhao, A. R. Paris, D. Kim, P. Yang, O. M. Yaghi and C. J. Chang, *Science*, 2015, **349**, 1208–1213.
85 Y. Zhang, L. Li, S. X. Guo, X. Zhang, F. Li, A. M. Bond and J. Zhang, *ChemSusChem*, 2020, **13**, 59–77.
86 D. Voiry, H. S. Shin, K. P. Loh and M. Chhowalla, *Nat. Rev. Chem.*, 2018, **2**, 0105.
87 S. Gao, Z. Sun, W. Liu, X. Jiao, X. Zu, Q. Hu, Y. Sun, T. Yao, W. Zhang, S. Wei and Y. Xie, *Nat. Commun.*, 2017, **8**, 14503.
88 S. Chen, H. Wang, Z. Kang, S. Jin, X. Zhang, X. Zheng, Z. Qi, J. Zhu, B. Pan and Y. Xie, *Nat. Commun.*, 2019, **10**, 788.
89 C. Peng, G. Luo, J. Zhang, M. Chen, Z. Wang, T. K. Sham, L. Zhang, Y. Li and G. Zheng, *Nat. Commun.*, 2021, **12**, 1580.
90 S. Siahrostami, K. Jiang, M. Karamad, K. R. Chan, H. T. Wang and J. Norskov, *ACS Sustainable Chem. Eng.*, 2017, **5**, 11080–11085.
91 H. Terrones, R. Lv, M. Terrones and M. S. Dresselhaus, *Rep. Prog. Phys.*, 2012, **75**, 062501.
92 Z. Y. Shu, G. Y. Ye, J. Wang, S. Q. Liu, Z. He, W. W. Zhu, B. Liu and M. Liu, *Ionics*, 2021, **27**, 3089–3098.
93 S. Back, M. S. Yeom and Y. Jung, *ACS Catal.*, 2015, **5**, 5089–5096.
94 F. Li, M. Xue, J. Li, X. Ma, L. Chen, X. Zhang, D. R. MacFarlane and J. Zhang, *Angew. Chem., Int. Ed.*, 2017, **56**, 14718–14722.
95 S. Liu, H. Tao, L. Zeng, Q. Liu, Z. Xu, Q. Liu and J. L. Luo, *J. Am. Chem. Soc.*, 2017, **139**, 2160–2163.
96 J. Wu, M. Liu, P. P. Sharma, R. M. Yadav, L. Ma, Y. Yang, X. Zou, X. D. Zhou, R. Vajtai, B. I. Yakobson, J. Lou and P. M. Ajayan, *Nano Lett.*, 2016, **16**, 466–470.
97 Y. Liu, J. Zhao and Q. Cai, *Phys. Chem. Chem. Phys.*, 2016, **18**, 5491–5498.
98 N. Sreekanth, M. A. Nazrulla, T. V. Vineesh, K. Sailaja and K. L. Phani, *Chem. Commun.*, 2015, **51**, 16061–16064.
99 C. M. Zhao, Y. Wang, Z. J. Li, W. X. Chen, Q. Xu, D. S. He, D. S. Xi, Q. H. Zhang, T. W. Yuan, Y. T. Qu, J. Yang, F. Y. Zhou, Z. K. Yang, X. Q. Wang, J. Wang, J. Luo, Y. F. Li, H. H. Duan, Y. Wu and Y. D. Li, *Joule*, 2019, **3**, 584–594.
100 C. Zhang, S. Yang, J. Wu, M. Liu, S. Yazdi, M. Ren, J. Sha, J. Zhong, K. Nie, A. S. Jalilov, Z. Li, H. Li, B. I. Yakobson, Q. Wu, E. Ringe, H. Xu, P. M. Ajayan and J. M. Tour, *Adv. Energy Mater.*, 2018, **8**, 1703487.
101 J. Wang, X. Huang, S. Xi, J. M. Lee, C. Wang, Y. Du and X. Wang, *Angew. Chem., Int. Ed.*, 2019, **58**, 13532–13539.
102 Q. Li, W. L. Zhu, J. J. Fu, H. Y. Zhang, G. Wu and S. H. Sun, *Nano Energy*, 2016, **24**, 1–9.
103 K. Jiang, S. Siahrostami, T. T. Zheng, Y. F. Hu, S. Hwang, E. Stavitski, Y. D. Peng, J. Dynes, M. Gangisetty, D. Su, K. Attenkofer and H. T. Wang, *Energy Environ. Sci.*, 2018, **11**, 893–903.
104 F. Li, G. H. Gu, C. Choi, P. Kolla, S. Hong, T. S. Wu, Y. L. Soo, J. Masa, S. Mukerjee, Y. S. Jung, J. S. Qiu and Z. Y. Sun, *Appl. Catal., B*, 2020, **277**, 119241.
105 M. G. Kibria, J. P. Edwards, C. M. Gabardo, C. T. Dinh, A. Seifitokaldani, D. Sinton and E. H. Sargent, *Adv. Mater.*, 2019, **31**, e1807166.
106 K. Liu, W. A. Smith and T. Burdyny, *ACS Energy Lett.*, 2019, **4**, 639–643.
107 T. Haas, R. Krause, R. Weber, M. Demler and G. Schmid, *Nat. Catal.*, 2018, **1**, 32–39.
108 H. Zhong, M. Ghorbani-Asl, K. H. Ly, J. Zhang, J. Ge, M. Wang, Z. Liao, D. Makarov, E. Zschech, E. Brunner, I. M. Weidinger, J. Zhang, A. V. Krasheninnikov, S. Kaskel, R. Dong and X. Feng, *Nat. Commun.*, 2020, **11**, 1409.
109 J. J. Velasco-Velez, R. V. Mom, L. E. Sandoval-Diaz, L. J. Falling, C. H. Chuang, D. Gao, T. E. Jones, Q. Zhu, R. Arrigo, B. Roldán Cuenya, A. Knop-Gericke, T. Lunkenbein and R. Schlogl, *ACS Energy Lett.*, 2020, **5**, 2106–2111.
110 J. B. Vennekoetter, R. Sengpiel and M. Wessling, *Chem. Eng. J.*, 2019, **364**, 89–101.
111 F. P. Garcia de Arquer, C. T. Dinh, A. Ozden, J. Wicks, C. McCallum, A. R. Kirmani, D. H. Nam, C. Gabardo, A. Seifitokaldani, X. Wang, Y. C. Li, F. Li, J. Edwards, L. J. Richter, S. J. Thorpe, D. Sinton and E. H. Sargent, *Science*, 2020, **367**, 661–666.
112 L. Li, A. Ozden, S. Guo, F. P. GarcíA De Arquer, C. Wang, M. Zhang, J. Zhang, H. Jiang, W. Wang, H. Dong, D. Sinton, E. H. Sargent and M. Zhong, *Nat. Commun.*, 2021, **12**, 5223.
113 D. Kim, W. Choi, H. W. Lee, S. Y. Lee, Y. Choi, D. K. Lee, W. Kim, J. Na, U. Lee, Y. J. Hwang and D. H. Won, *ACS Energy Lett.*, 2021, **6**, 3488–3495.
114 C. Xia, P. Zhu, Q. Jiang, Y. Pan, W. T. Liang, E. Stavitsk, H. N. Alshareef and H. T. Wang, *Nat. Energy*, 2019, **4**, 776–785.
115 P. Zhu, C. Xia, C.-Y. Liu, K. Jiang, G. Gao, X. Zhang, Y. Xia, Y. Lei, H. N. Alshareef, T. P. Senftle and H. Wang, *Proc. Natl. Acad. Sci. U. S. A.*, 2021, **118**, e2010868118.
116 L. Fan, C. Xia, P. Zhu, Y. Lu and H. Wang, *Nat. Commun.*, 2020, **11**, DOI: 10.1038/s41467-020-17403-1.
117 S. F. Tan, S. W. Chee, Z. Baraissov, H. M. Jin, T. L. Tan and U. Mirsaidov, *Adv. Funct. Mater.*, 2019, **29**, 1903242.
118 J. Yin, S. Y. Shan, L. F. Yang, D. Mott, O. Malis, V. Petkov, F. Cai, M. S. Ng, J. Luo, B. H. Chen, M. Engelhard and C. J. Zhong, *Chem. Mater.*, 2012, **24**, 4662–4674.
119 T. Avanesian, S. Dai, M. J. Kale, G. W. Graham, X. Pan and P. Christopher, *J. Am. Chem. Soc.*, 2017, **139**, 4551–4558.

120 W. Zhan, J. Wang, H. Wang, J. Zhang, X. Liu, P. Zhang, M. Chi, Y. Guo, Y. Guo, G. Lu, S. Sun, S. Dai and H. Zhu, *J. Am. Chem. Soc.*, 2017, **139**, 8846–8854.
121 M. D. Argyle and C. H. Bartholomew, *Catalysts*, 2015, **5**, 145–269.
122 S. Popovic, M. Smiljanic, P. Jovanovic, J. Vavra, R. Buonsanti and N. Hodnik, *Angew. Chem., Int. Ed.*, 2020, **59**, 14736–14746.
123 D. Karapinar, N. T. Huan, N. Ranjbar Sahraie, J. Li, D. Wakerley, N. Touati, S. Zanna, D. Taverna, L. H. Galvão Tizei, A. Zitolo, F. Jaouen, V. Mougel and M. Fontecave, *Angew. Chem., Int. Ed.*, 2019, **58**, 15098–15103.
124 S. W. Chee, T. Lunkenbein, R. Schlogl and B. R. Cuenya, *J. Phys.: Condens. Matter*, 2021, **33**, 153001.
125 Y. Zhu, J. Wang, H. Chu, Y.-C. Chu and H. M. Chen, *ACS Energy Lett.*, 2020, **5**, 1281–1291.
126 M. A. Bañares, *Catal. Today*, 2005, **100**, 71–77.
127 A. Preet and T. E. Lin, *Catalysts*, 2021, **11**, 594.
128 F. D. Mayer, P. Hosseini-Benhangi, C. M. Sanchez-Sanchez, E. Asselin and E. L. Gyenge, *Commun. Chem.*, 2020, **3**, 155.
129 S. Narayanaru, J. Chinnaiah, K. L. Phani and F. Scholz, *Electrochim. Acta*, 2018, **264**, 269–274.
130 C. I. Shaughnessy, D. T. Jantz and K. C. Leonard, *J. Mater. Chem. A*, 2017, **5**, 22743–22749.
131 T. Kai, M. Zhou, Z. Duan, G. A. Henkelman and A. J. Bard, *J. Am. Chem. Soc.*, 2017, **139**, 18552–18557.
132 D. T. Jantz and K. C. Leonard, *Ind. Eng. Chem. Res.*, 2018, **57**, 7431–7440.
133 Y. Kim, A. Jo, Y. Ha, Y. Lee, D. Lee, Y. Lee and C. Lee, *Electroanalysis*, 2018, **30**, 2861–2868.
134 N. Sreekanth and K. L. Phani, *Chem. Commun.*, 2014, **50**, 11143–11146.
135 L. I. Stephens, N. A. Payne and J. Mauzeroll, *Anal. Chem.*, 2020, **92**, 3958–3963.
136 D. Polcari, P. Dauphin-Ducharme and J. Mauzeroll, *Chem. Rev.*, 2016, **116**, 13234–13278.
137 D. Wang and L. J. Wan, *J. Phys. Chem. C*, 2007, **111**, 16109–16130.
138 H. Feng, X. Xu, Y. Du and S. X. Dou, *Electrochem. Energy Rev.*, 2021, **4**, 249–268.
139 Y. Liang, J. H. K. Pfisterer, D. McLaughlin, C. Csoklich, L. Seidl, A. S. Bandarenka and O. Schneider, *Small Methods*, 2019, **3**, 1800387.
140 C. F. Tsang, A. C. Javier, Y.-G. Kim, J. H. Baricuatro, K. D. Cummins, J. Kim, G. Jerkiewicz, J. C. Hemminger and M. P. Soriaga, *J. Electrochem. Soc.*, 2018, **165**, J3350–J3354.
141 Y.-G. Kim and M. P. Soriaga, *J. Electroanal. Chem.*, 2014, **734**, 7–9.
142 Y.-G. Kim, J. H. Baricuatro, A. Javier, J. M. Gregoire and M. P. Soriaga, *Langmuir*, 2014, **30**, 15053–15056.
143 G. H. Simon, C. S. Kley and B. Roldán Cuenya, *Angew. Chem., Int. Ed.*, 2021, **60**, 2561–2568.
144 M. R. Nellist, F. A. L. Laskowski, J. J. Qiu, H. Hajibabaei, K. Sivula, T. W. Hamann and S. W. Boettcher, *Nat. Energy*, 2018, **3**, 46–52.
145 P. Grosse, D. Gao, F. Scholten, I. Sinev, H. Mistry and B. Roldán Cuenya, *Angew. Chem., Int. Ed.*, 2018, **57**, 6192–6197.
146 Y. A. Wu, Z. Yin, M. Farmand, Y.-S. Yu, D. A. Shapiro, H.-G. Liao, W.-I. Liang, Y.-H. Chu and H. Zheng, *Sci. Rep.*, 2017, **7**, 42527.
147 Y. A. Wu, L. Li, Z. Li, A. Kinaci, M. K. Y. Chan, Y. Sun, J. R. Guest, I. McNulty, T. Rajh and Y. Liu, *ACS Nano*, 2016, **10**, 3738–3746.
148 Y. A. Wu, I. McNulty, C. Liu, K. C. Lau, Q. Liu, A. P. Paulikas, C. J. Sun, Z. H. Cai, J. R. Guest, Y. Ren, V. Stamenkovic, L. A. Curtiss, Y. Z. Liu and T. Rajh, *Nat. Energy*, 2019, **4**, 957–968.
149 B. D. A. Levin, D. Haiber, Q. Liu and P. A. Crozier, *Microsc. Microanal.*, 2020, **26**, 134–138.
150 K. Jungjohann and C. B. Carter, in *Transmission Electron Microscopy*, Springer International Publishing, 2016, pp. 17–80, DOI: 10.1007/978-3-319-26651-0_2.
151 M. J. Williamson, R. M. Tromp, P. M. Vereecken, R. Hull and F. M. Ross, *Nat. Mater.*, 2003, **2**, 532–536.
152 E. Fahrenkrug, D. H. Alsem, N. Salmon and S. Maldonado, *J. Electrochem. Soc.*, 2017, **164**, H358–H364.
153 X. Wang, K. Klingan, M. Klingenhof, T. Möller, J. Ferreira de Araújo, I. Martens, A. Bagger, S. Jiang, J. Rossmeisl, H. Dau and P. Strasser, *Nat. Commun.*, 2021, **12**, 794.
154 J. Vavra, T. H. Shen, D. Stoian, V. Tileli and R. Buonsanti, *Angew. Chem., Int. Ed.*, 2021, **60**, 1347–1354.
155 D. A. Shapiro, Y.-S. Yu, T. Tyliszczak, J. Cabana, R. Celestre, W. Chao, K. Kaznatcheev, A. L. D. Kilcoyne, F. Maia, S. Marchesini, Y. S. Meng, T. Warwick, L. L. Yang and H. A. Padmore, *Nat. Photonics*, 2014, **8**, 765–769.
156 J. Deng, D. J. Vine, S. Chen, Y. S. G. Nashed, Q. Jin, N. W. Phillips, T. Peterka, R. Ross, S. Vogt and C. J. Jacobsen, *Proc. Natl. Acad. Sci. U. S. A.*, 2015, **112**, 2314–2319.
157 T. H. Yoon, *Appl. Spectrosc. Rev.*, 2009, **44**, 91–122.
158 B. Rösner, S. Finizio, F. Koch, F. Döring, V. A. Guzenko, M. Langer, E. Kirk, B. Watts, M. Meyer, J. Loroña Ornelas, A. Späth, S. Stanescu, S. Swaraj, R. Belkhou, T. Ishikawa, T. F. Keller, B. Gross, M. Poggio, R. H. Fink, J. Raabe, A. Kleibert and C. David, *Optica*, 2020, **7**, 1602–1608.
159 S. Finizio, S. Mayr and J. Raabe, *J. Synchrotron Radiat.*, 2020, **27**, 1320–1325.
160 E. De Smit, I. Swart, J. F. Creemer, G. H. Hoveling, M. K. Gilles, T. Tyliszczak, P. J. Kooyman, H. W. Zandbergen, C. Morin, B. M. Weckhuysen and F. M. F. De Groot, *Nature*, 2008, **456**, 222–225.
161 D. Guay, J. Stewart-Ornstein, X. Zhang and A. P. Hitchcock, *Anal. Chem.*, 2005, **77**, 3479–3487.
162 A. Ulvestad, A. Singer, J. N. Clark, H. M. Cho, J. W. Kim, R. Harder, J. Maser, Y. S. Meng and O. G. Shpyrko, *Science*, 2015, **348**, 1344–1347.
163 I. Robinson and R. Harder, *Nat. Mater.*, 2009, **8**, 291–298.

164 M. Abuin, Y. Y. Kim, H. Runge, S. Kulkarni, S. Maier, D. Dzhigaev, S. Lazarev, L. Gelisio, C. Seitz, M. I. Richard, T. Zhou, V. Vonk, T. F. Keller, I. A. Vartanyants and A. Stierle, *ACS Appl. Nano Mater.*, 2019, **2**, 4818–4824.
165 R. Harder, M. Liang, Y. Sun, Y. Xia and I. K. Robinson, *New J. Phys.*, 2010, **12**, 035019.
166 W. Cha, A. Ulvestad, M. Allain, V. Chamard, R. Harder, S. J. Leake, J. Maser, P. H. Fuoss and S. O. Hruszkewycz, *Phys. Rev. Lett.*, 2016, **117**, 225501.
167 I. Robinson, J. Clark and R. Harder, *J. Opt.*, 2016, **18**, 054007.
168 A. Ulvestad, A. Tripathi, S. O. Hruszkewycz, W. Cha, S. M. Wild, G. B. Stephenson and P. H. Fuoss, *Phys. Rev. B*, 2016, **93**, 184105.
169 R. P. Jansonius, L. M. Reid, C. N. Virca and C. P. Berlinguette, *ACS Energy Lett.*, 2019, **4**, 980–986.
170 S. Fernández, L. Gao, J. P. Hofmann, J. Carnis, S. Labat, G. A. Chahine, A. J. F. Van Hoof, M. W. G. M. (Tiny) Verhoeven, T. U. Schülli, E. J. M. Hensen, O. Thomas and M.-I. Richard, *Nanoscale*, 2019, **11**, 331–338.
171 X. Zheng, B. Zhang, P. De Luna, Y. Liang, R. Comin, O. Voznyy, L. Han, F. P. García de Arquer, M. Liu, C. T. Dinh, T. Regier, J. J. Dynes, S. He, H. L. Xin, H. Peng, D. Prendergast, X. Du and E. H. Sargent, *Nat. Chem.*, 2018, **10**, 149–154.
172 J. Timoshenko and B. Roldán Cuenya, *Chem. Rev.*, 2021, **121**, 882–961.
173 M. Benfatto and C. Meneghini, in *Synchrotron Radiation*, Springer Berlin Heidelberg, 2015, ch. 7, pp. 213–240, DOI: 10.1007/978-3-642-55315-8_7.
174 J. J. Velasco-Velez, C. H. Wu, T. A. Pascal, L. F. Wan, J. Guo, D. Prendergast and M. Salmeron, *Science*, 2014, **346**, 831–834.
175 P. De Luna, R. Quintero-Bermudez, C.-T. Dinh, M. B. Ross, O. S. Bushuyev, P. Todorović, T. Regier, S. O. Kelley, P. Yang and E. H. Sargent, *Nat. Catal.*, 2018, **1**, 103–110.
176 J. Wang, C. Cheng, B. Huang, J. Cao, L. Li, Q. Shao, L. Zhang and X. Huang, *Nano Lett.*, 2021, **21**, 980–987.
177 L. P. Zhong, D. K. Chen and S. Zafeiratos, *Catal. Sci. Technol.*, 2019, **9**, 3851–3867.
178 K. Roy, L. Artiglia and J. A. van Bokhoven, *ChemCatChem*, 2018, **10**, 666–682.
179 A. Kolmakov, D. A. Dikin, L. J. Cote, J. Huang, M. K. Abyaneh, M. Amati, L. Gregoratti, S. Gunther and M. Kiskinova, *Nat. Nanotechnol.*, 2011, **6**, 651–657.
180 M. Favaro, H. Xiao, T. Cheng, W. A. Goddard 3rd, J. Yano and E. J. Crumlin, *Proc. Natl. Acad. Sci. U. S. A.*, 2017, **114**, 6706–6711.
181 J. Kim, H. Ha, W. H. Doh, K. Ueda, K. Mase, H. Kondoh, B. S. Mun, H. Y. Kim and J. Y. Park, *Nat. Commun.*, 2020, **11**, 5649.
182 R. Blume, D. Rosenthal, J. P. Tessonnier, H. N. Li, A. Knop-Gericke and R. Schlogl, *ChemCatChem*, 2015, **7**, 2871–2881.
183 U. Bergmann, J. Kern, R. W. Schoenlein, P. Wernet, V. K. Yachandra and J. Yano, *Nat. Rev. Phys.*, 2021, **3**, 264–282.
184 I. Matsuda and Y. Kubota, *Chem. Lett.*, 2021, **50**, 1336–1344.
185 G. Geloni, Z. Huang and C. Pellegrini, in *X-Ray Free Electron Lasers*, The Royal Society of Chemistry, 2017, pp. 1–44, DOI: 10.1039/9781782624097-00001.
186 C. Pellegrini, A. Marinelli and S. Reiche, *Rev. Mod. Phys.*, 2016, **88**, 015006.
187 J. Yang, R. Dettori, J. P. F. Nunes, N. H. List, E. Biasin, M. Centurion, Z. Chen, A. A. Cordones, D. P. Deponte, T. F. Heinz, M. E. Kozina, K. Ledbetter, M.-F. Lin, A. M. Lindenberg, M. Mo, A. Nilsson, X. Shen, T. J. A. Wolf, D. Donadio, K. J. Gaffney, T. J. Martinez and X. Wang, *Nature*, 2021, **596**, 531–535.
188 A. H. Zewail, *Science*, 1988, **242**, 1645–1653.
189 L. B. Hoch, P. Szymanski, K. K. Ghuman, L. He, K. Liao, Q. Qiao, L. M. Reyes, Y. Zhu, M. A. El-Sayed, C. V. Singh and G. A. Ozin, *Proc. Natl. Acad. Sci. U. S. A.*, 2016, **113**, E8011–E8020.
190 J. Sá and J. Szlachetko, *Catal. Lett.*, 2013, **144**, 197–203.
191 E. L. Clark, M. R. Singh, Y. Kwon and A. T. Bell, *Anal. Chem.*, 2015, **87**, 8013–8020.
192 E. L. Clark and A. T. Bell, *J. Am. Chem. Soc.*, 2018, **140**, 7012–7020.
193 T. Herl and F. M. Matysik, *ChemElectroChem*, 2020, **7**, 2498–2512.
194 M. Plodinec, H. C. Nerl, R. Farra, M. G. Willinger, E. Stotz, R. Schlogl and T. Lunkenbein, *Microsc. Microanal.*, 2020, **26**, 220–228.
195 J. Lu, X. Hua and Y. T. Long, *Analyst*, 2017, **142**, 691–699.
196 R. Kas, O. Ayemoba, N. J. Firet, J. Middelkoop, W. A. Smith and A. Cuesta, *ChemPhysChem*, 2019, **20**, 2904–2925.
197 F. Zaera, *Chem. Soc. Rev.*, 2014, **43**, 7624–7663.
198 A. J. Wain and M. A. O'Connell, *Adv. Phys.: X*, 2017, **2**, 188–209.
199 J. Heyes, M. Dunwell and B. Xu, *J. Phys. Chem. C*, 2016, **120**, 17334–17341.
200 C. Hess, *Chem. Soc. Rev.*, 2021, **50**, 3519–3564.
201 Y. Wang, Y. Li, J. Liu, C. Dong, C. Xiao, L. Cheng, H. Jiang, H. Jiang and C. Li, *Angew. Chem.*, 2021, **60**, 7681–7685.
202 J. F. Li, Y. F. Huang, Y. Ding, Z. L. Yang, S. B. Li, X. S. Zhou, F. R. Fan, W. Zhang, Z. Y. Zhou, D. Y. Wu, B. Ren, Z. L. Wang and Z. Q. Tian, *Nature*, 2010, **464**, 392–395.
203 Z. Zhang, S. Sheng, R. Wang and M. Sun, *Anal. Chem.*, 2016, **88**, 9328–9346.
204 N. Kumar, C. S. Wondergem, A. J. Wain and B. M. Weckhuysen, *J. Phys. Chem. Lett.*, 2019, **10**, 1669–1675.
205 E. Pérez-Gallent, G. Marcandalli, M. C. Figueiredo, F. Calle-Vallejo and M. T. M. Koper, *J. Am. Chem. Soc.*, 2017, **139**, 16412–16419.

206 S. Lee, D. Kim and J. Lee, *Angew. Chem.*, 2015, **127**, 14914–14918.
207 A. S. Varela, W. Ju, T. Reier and P. Strasser, *ACS Catal.*, 2016, **6**, 2136–2144.
208 D. Bohra, J. H. Chaudhry, T. Burdyny, E. A. Pidko and W. A. Smith, *Energy Environ. Sci.*, 2019, **12**, 3380–3389.
209 Y. Wang, M. Hatakeyama, K. Ogata, M. Wakabayashi, F. Jin and S. Nakamura, *Phys. Chem. Chem. Phys.*, 2015, **17**, 23521–23531.
210 S. Banerjee, X. Han and V. S. Thoi, *ACS Catal.*, 2019, **9**, 5631–5637.
211 L. Zhang, Z. C. Wei, S. Thanneeru, M. Meng, M. Kruzyk, G. Ung, B. Liu and J. He, *Angew. Chem., Int. Ed.*, 2019, **58**, 15834–15840.
212 A. K. Buckley, M. Lee, T. Cheng, R. V. Kazantsev, D. M. Larson, W. A. Goddard III, F. D. Toste and F. M. Toma, *J. Am. Chem. Soc.*, 2019, **141**, 7355–7364.
213 A. Wagner, C. D. Sahm and E. Reisner, *Nat. Catal.*, 2020, **3**, 775–786.
214 A. Khorshidi, J. Violet, J. Hashemi and A. A. Peterson, *Nat. Catal.*, 2018, **1**, 263–268.
215 Z. Dai, L. Liu and Z. Zhang, *Adv. Mater.*, 2019, **31**, 1805417.